Patient-derived xenograft culture-transplant system for investigation of human breast cancer metastasis

Dennis Ma[2†], Grace A. Hernandez[1†], Austin E.Y.T. Lefebvre[3], Hamad Alshetaiwi[2,4], Kerrigan Blake[5], Kushal R. Dave[1], Maha Rauf[2], Justice W. Williams[2], Ryan T. Davis[1], Katrina T. Evans[1], Madona Y.G. Masoud[1], Regis Lee[1], Robert A. Edwards[6], Michelle A. Digman[3], Kai Kessenbrock[2*], and Devon A. Lawson[1*]

[1]Department of Physiology and Biophysics, University of California, Irvine, Irvine, CA 92617

[2]Department of Biological Chemistry, University of California, Irvine, Irvine, CA 92617

[3]Department of Biomedical Engineering, University of California, Irvine, Irvine, CA 92617

[4]Department of Pathology, University of Hail, Hail, 2440, Saudi Arabia

[5]Center for Complex Biological Systems, University of California, Irvine, Irvine, CA 92697

[6]Department of Pathology & Laboratory Medicine, University of California, Irvine, CA 92617

[†]Authors contributed equally
*Address correspondence to

Devon A. Lawson, Ph.D.
Department of Physiology and Biophysics
University of California, Irvine
839 Health Sciences Road, Sprague Hall 112
Irvine, CA 92617-3905
Tel: 949-824-4113
email: dalawson@uci.edu

Kai Kessenbrock
Department of Biological Chemistry
University of California, Irvine
839 Health Science Road, Sprague Hall 114
Irvine, CA 92697-3905
Tel: 949-824-4113
Email: kai.kessenbrock@uci.edu

KEYWORDS:
Breast cancer, metastasis, patient-derived xenograft, PDX, 3D, sphere culture, NME1, oligomycin, oxidative phosphorylation

Abstract

Metastatic disease carries a poor prognosis and its study is limited by the availability of authentic experimental models. Here, we present a 3D tumor sphere culture-transplant system that facilitates expansion and modulation of patient-derived xenograft (PDX) cells for use in functional experimental metastasis assays. RNA sequencing shows PDX tumor spheres maintain fundamental properties of native tumor cells. *In vivo* transplantation studies demonstrate cultured cells yield robust spontaneous and experimental metastasis following orthotopic and intravenous or intracardiac delivery, respectively. Pharmacologic inhibition of previously reported metastasis-promoting pathways also inhibits metastasis of PDX cells after culture, validating our approach. Finally, we used our culture-transplant system to demonstrate a new role of the metabolic enzyme NME1 in promoting breast cancer metastasis. Thus, we present a novel method for authentic propagation, engineering and transplantation of PDX models for functional studies of metastasis using bona fide patient tumor cells.

Introduction

More than 95% of breast cancer mortality is seen in patients with metastatic diease[1,2]. There are limited effective treatments for metastasis, and identification of new therapeutic targets has been hindered by lack of experimental models that faithfully recapitulate metastatic disease *ex vivo*. Most metastasis research has been conducted with a handful of genetically engineered mouse models (GEMM) and cell lines that have limitations for accurately modeling metastasis in humans[3,4]. Patient-derived xenograft (PDX) models, where patient tumors are propagated in mice, offer increased authenticity as they maintain intratumoral heterogeneity, molecular markers and pathological characteristics of the original patient tumor[5–7]. PDX models have been used extensively in pre-clinical studies for drug testing but their use in metastasis research has been limited by technical challenges. Primary tumor cells are notoriously challenging to maintain in their native biological state *in vitro*. Studies have reported transient cultures of PDX cells for pre-clinical drug testing[8–10], but typically support short term studies (24-72 hours) and have not been optimized for extended culture essential for viral engineering and cell expansion for *in vivo* metastasis assays. In this report, we address this issue by optimizing culture conditions for growth, genetic engineering, chemical modulation, expansion and subsequent transplantation of PDX cells to facilitate critical investigations into mechanisms driving metastasis.

We screened three dimensional (3D) culture conditions shown to propagate breast epithelial and tumor cells[8,11,12], and present an optimized method for propagating PDX cells as tumor spheres. RNA sequencing (RNA-seq) analysis shows PDX tumor sphere cells maintain gene expression signatures characteristic of uncultured PDX tumor cells. These cultured cells can be robustly engineered with lentivirus and viably expanded for subsequent transplantation *in vivo*. Orthotopic transplantation of cultured and engineered tumor sphere cells results in outgrowth of tumors that recapitulate native PDX tumors. We find that PDX tumor sphere cells

yield robust metastasis following orthotopic, intravenous (i.v.) and intracardiac (i.c.) injection *in vivo*, and inhibition of pathways known to attenuate metastasis[13] yields corroborating results after sphere culture. Finally, we demonstrate our approach can be used to investigate the function of new genes in metastatic progression. Thus, we present this PDX tumor sphere culture-transplant system as an important new approach enabling genetic engineering and functional evaluations of patient tumor cells for metastasis research.

Results

Development of a 3D culture system for viable propagation of PDX cells as tumor spheres in vitro

We screened 3D culture conditions to develop a robust method for viable expansion of PDX tumor cells *in vitro* (Fig. 1a). We assessed two 3D conditions: 1) ultra-low attachment (ULA) plates that support growth in suspension[14,15], and 2) Matrigel, a gelatinous basement membrane preparation that supports growth in semi-solid substratum[16] (Fig. 1a). We also tested two media conditions: 1) Mammary Epithelial Cell Growth Medium (MEGM), which supports short-term cultures of PDX cells for drug testing[8], and 2) EpiCult^{TM}-B (EpiCult), which is commonly used for breast epithelial cell culture[17,18] (Fig. 1a).

We used previously established breast cancer PDX models, HCI001, HCI002, HCI010 ($ER^-PR^-Her2^-$, basal-like), and HCI011 ($ER^+PR^+Her2^-$, luminal B)[5] (Fig. 1a). We first screened culture conditions using the HCI010 model and validated the results using the other three. HCI010 tumors were harvested from PDX mice after 2-5 months growth, digested to single cell suspensions and plated into four culture conditions: i) ULA plates and EpiCult (ULA-E); ii) ULA plates and MEGM (ULA-M); iii) Matrigel and EpiCult (MAT-E); and iv) Matrigel with MEGM (MAT-M) (Fig. 1a). Microscopy 7-14 days later showed ULA-E and MAT-E both produced spheroid structures, while ULA-M and MAT-M produced limited growth (Fig. 1b), providing an indication that MEGM is insufficient to support growth of PDX cells.

We analyzed cell viability by trypan blue exclusion assay, and annexin V (aV) and propidium iodide (PI) staining by flow cytometry. Trypan blue exclusion showed ULA-E produced the highest viability (85.9 ± 3.6%), and MAT-M showed the lowest (25.5 ± 3.9%; $p<0.0001$) (Fig. 1c). aV and PI staining yielded more detailed differences in cell viability, as this assay is able to discriminate viable (aV^-PI^-) cells from early apoptotic (aV^+PI^-) and late apoptotic/necrotic (PI^+) cells[19]. aV and PI staining showed MAT-E produced the highest percentage of aV^-PI^- viable cells (60.6 ± 2.0%), followed by ULA-E (26.3 ± 3%) which was 2.3-fold lower than MAT-E ($p<0.0001$) (Fig. 1d, Supplementary Figure 1a)). ULA-E also showed 1.4-fold percent more aV^+PI^- cells in early apoptosis than MAT-E ($p=.0014$) (Fig. 1d), further indicating MAT-E is superior to ULA-E for producing viable PDX sphere growth.

We next compared culture conditions for their ability to expand and passage PDX cells. The numbers of live HCI010 cells were compared before plating and after nine days of culture. Cell counts showed MAT-E produced the greatest expansion of HCI010 cells (2.2-fold), while ULA-E (1.3-fold) and the other conditions produced minimal or negative expansion ($p<0.0001$) (Fig. 1e). Passaging experiments showed MAT-E could also support extended viable growth of PDX cells. First generation (P0) HCI010 spheres were harvested, dissociated and re-plated for an additional 14-17 days to produce P1 spheres (Fig. 1f). Trypan blue exclusion and aV and PI staining of P1 sphere cells showed that MAT-E produced P1 cells with excellent viability (62.7 ± 7.7% trypan blue, 87.1 ± 1.7% aV^-PI^-) (Fig. 1g,h). Live cell counts before plating and after 21 days of culture also showed that MAT-E was able to support a further 2-fold expansion of HCI010 cells (Fig. 1i). These data show that MAT-E produces both the greatest viable sphere growth and expansion of PDX cells.

Finally, we investigated whether MAT-E could support the growth of other PDX models, and whether spheres are generated from human tumor cells and not contaminating mouse epithelium. HCI001, HCI002 and HCI011 tumors were harvested from PDX mice, dissociated to single cell suspensions and plated in MAT-E conditions. Microscopy revealed that MAT-E

produced sphere outgrowth from all three PDX models (Supplementary Fig 1c). Species identity of sphere cells was evaluated using species-specific antibodies for CD298 (human) and MHC-I (mouse) using a flow cytometry assay previously developed by our laboratory[20]. This confirmed sphere cells were nearly entirely derived from $CD298^{+}MHC\text{-}I^{-}$ human tumor cells (98.8% HCI010; 94.5% HCI002; 91.9% HCI001; 98.7% HCI011) (Supplementary Fig 1d). These data show that MAT-E is most suitable for expanding human tumor cells from PDX models. Supplementary videos 1-3 further show sphere growth in MAT-E conditions using time lapse imaging.

PDX tumor sphere cells maintain cellular identity and authenticity *in vitro*

We performed bulk RNA-seq of $CD298^{+}MHC\text{-}I^{-}$ uncultured and cultured (14 days) HCI010 and HCI002 PDX cells to investigate whether MAT-E conditions maintain cellular identity and authenticity of PDX cells (Fig. 2a). We performed differential expression analysis using the package *DESeq2*[21], followed by the Pearson's correlation test, which revealed a strong correlation between genes expressed in uncultured and cultured cells, with correlation values of 0.82, 0.70, and 0.83 for HCI010 and 0.48, 0.70, and 0.88 for HCI002 (Fig. 2b). These results indicate MAT-E culture conditions do not cause substantial changes in gene expression and maintain cellular identity and authenticity of PDX cells.

We investigated top genes upregulated and downregulated in cultured cells across both patient datasets. Of the 22,446 genes, differential expression analysis identified 1,732 significant differentially expressed genes with at least two-fold change in expression, including 277 genes upregulated and 1,455 genes downregulated in cultured cells compared to uncultured (Supplementary Table 1, Fig. 2c). CXCL8, CXCL1, and CXCL5 were among the top genes upregulated in cultured cells (Fig. 2c). These genes are part of the CXC chemokine family, play a role in immune cell recruitment, and are known regulators of angiogenesis in normal and diseased states, including cancer[22–25].

Gene Ontology (GO) analysis of 277 genes upregulated in cultured cells revealed 'cytokine-mediated signaling pathway' and 'neutrophil activation involved in immune response' as top GO terms (Fig. 2d). CXCL8, CXCL1, CXCL5, and BST2 were among the upregulated genes associated with 'cytokine-mediated signaling pathway' (Fig. 2e). Cultured cells also had increased expression of genes associated with 'extracellular matrix organization', including COL6A1, COL6A2, and LAMC2 (Fig. 2e), which encode for collagens and laminin, the main extracellular components in Matrigel[26]. Interestingly, cultured cells also had increased expression of genes associated with 'epithelial to mesenchymal transition' (EMT), including WNT5A, TGFB1, S100A4, and LOXL2 (Fig. 2e). These results suggest MAT-E culture conditions may be promoting immune response pathways, as well as upregulating production of extracellular matrix components. Additionally, there is a distinct EMT signature in cultured PDX cells.

Lastly, we investigated changes in gene expression of ERBB2 (HER2), ESR1, ESR2, and PGR which encode for erb-b2 receptor tyrosine kinase 2, estrogen receptor 1 and 2, and progesterone receptor, respectively. HCI002 and HCI010 tumor grafts were derived from triple-negative, basal-like breast tumors and therefore, lack these receptors[27]. We found ERBB2, ESR1, and ESR1 were not significantly differentially expressed between uncultured and cultured. Additionally, PGR was not present in our dataset. These results confirm MAT-E culture conditions do not induce changes in ERBB2 (HER2), ESR1, ESR2, and PGR in comparison to native HCI002 and HCI010 cells.

PDX tumor sphere cells maintain tumorigenic potential and form spontaneous metastasis *in vivo*

We investigated whether PDX cells maintain their capacity to form primary tumors and spontaneously metastasize following sphere culture. Spontaneous metastasis models are critical for functional studies evaluating the complete metastatic cascade from a primary tumor.

Prior work has shown the HCI010 model develops poorly differentiated, basal-like primary tumors and spontaneous lung metastasis in >90% of mice following orthotopic transplantation[5,20]. We cultured and expanded HCI010 cells in MAT-E for two weeks and orthotopically transplanted serial dilutions (5×10^3 - 3.0×10^5) of cells to determine their capacity to form primary tumors in NOD/SCID mice (Fig. 3a). Remarkably, we observed primary tumor growth from 100% of transplants (40/40) 8-14 weeks later (Fig. 3b). Similarly, ~96.8% (30/31) of animals transplanted with HCI002 MAT-E cells developed orthotopic tumors (Supplementary Fig. 2a).

We compared histopathological and molecular features of MAT-E-cultured and native PDX tumors and found they were indistinguishable by microscopy (Fig. 3c, Supplementary Fig 2b). Both native and MAT-E HCI010 tumors were poorly vascularized, necrotic and showed no epithelioid differentiation, showing little nodularity or ductal structure (Fig. 3c). HCI002 native and MAT-E tumors both showed scant intervening myxoid stroma and thin walled vessels, less necrosis, and retained some small areas of nodular aggregates but were mostly undifferentiated (Supplementary Fig 2b). Immunofluorescence (IF) staining of canonical basal (KRT5), myoepithelial (SMA) and luminal (KRT18) cell markers further indicated MAT-E tumors maintain their native differentiation state (Fig. 3c). Native and MAT-E HCI010 tumors displayed widespread KRT5 and KRT18 expression, and limited SMA expression, as expected for basal-like tumors (Fig. 3c).

We further evaluated distal tissues of orthotopically transplanted mice for spontaneous metastasis. HCI010 MAT-E cells (1×10^5) were transplanted orthotopically into NOD/SCID (n=14) and NSG (n=5) mice, which support different degrees of human cell engraftment. Distal tissues were harvested 60 days later and dissociated to produce single cell suspensions. Flow cytometry analysis of NOD/SCID mice identified $CD298^+MHC\text{-}I^-$ human metastatic cells in lungs (11/14), lymph nodes (5/14), bone marrow (2/5), and peripheral blood (2/5). Metastatic burden, determined by the percentage of $CD298^+MHC\text{-}I^-$ PDX cells of total cells in peripheral tissues,

was low in most tissues (lung, 0.020 ± 0.020%; lymph nodes, 1.222 ± 1.656%; bone marrow, 0.039 ± 0.048%; and peripheral blood, 0.011 ± 0.002%), consistent with reports for the native HCI010 model[20] (Fig. 3d). No metastasis was detected in brains (0/5). Interestingly, NSG mice displayed >32-fold higher metastatic burden in lungs compared to NOD/SCID mice ($p<0.0001$) (Supplementary Fig. 2c) with lesions detectable by histopathological analysis (Fig. 3e). This is consistent with reports demonstrating the importance of natural killer cells in controlling metastasis, which are absent in NSG mice, and shows different immunodeficient strains can be used to achieve specific study contexts[28]. Importantly, we also observed lung metastasis (5/5 mice; 0.172 ± 0.104%) and circulating tumor cells in peripheral blood (3/5 mice; 0.021 ± 0.017%) in mice transplanted with HCI002 MAT-E cells (Supplementary Fig. 2d,e) demonstrating the capacity for spontaneous metastasis is maintained after culture in other PDX models. Thus, PDX cells maintain their tumorigenic and metastatic potential after sphere culture, demonstrating our approach can be used for investigations of the complete metastatic cascade.

PDX tumor sphere cells can be genetically engineered for functional studies of metastasis *in vivo*

The ability to genetically manipulate genes of interest is critical to facilitate functional investigations of metastasis. We investigated whether PDX tumor sphere cells can be genetically engineered and transplanted to generate spontaneous metastasis *in vivo*. Using a GFP lentiviral construct (+GFP), we tested the infection efficiency of HCI002 and HCI010 sphere cells grown in MAT-E conditions (Fig. 4a). PDX cells were grown for 2-3 weeks to generate P0 spheres and were harvested and dissociated to generate cell suspensions. P0 cells were transduced using a combined centrifugation and suspension infection protocol (see Methods), and re-plated in MAT-E conditions for 2-3 weeks to expand transduced cells and generate P1 spheres (Fig. 4a). Fluorescence microscopy revealed robust and evenly distributed

GFP expression both within and between P1 spheres at low and high power (Fig. 4b,c). Quantification of infection efficiency by flow cytometry showed successful transduction with 75.2 ± 6.4% and 23.2 ± 7.6% of HCI010 and HCI002 cells positive for GFP, respectively (Fig. 4d).

We next determined whether transduced P1 sphere cells could retain GFP signal and produce spontaneous metastasis following orthotopic transplantation *in vivo*. Flow cytometry sorted GFP+ HCI002 and HCI010 P1 sphere cells were transplanted, and primary tumors and lungs were collected and analyzed 60 days later. Whole mount imaging showed that GFP expression was retained in primary tumors (Fig 4e), and quantification by flow cytometry showed that on average >92% of $CD298^{+}MHC\text{-}I^{-}$ human PDX tumor cells retained GFP signal (Fig 4f). Fluorescence microscopy of lung sections revealed GFP positive metastatic lesions (Fig 4g) and flow cytometry identified $CD298^{+}MHC\text{-}I^{-}GFP^{+}$ human metastatic cells in the lungs (Fig 4h). Remarkably, an average of >96% $CD298^{+}MHC\text{-}I^{-}$ of human metastatic cells retained GFP expression during spontaneous lung metastasis. Thus, we demonstrate PDX sphere cells can be robustly engineered, maintain their capacity to form primary tumors and spontaneous metastasis, and retain their genetic alterations *in vivo*.

PDX tumor sphere cells produce robust experimental metastasis *in vivo*

In experimental metastasis models, cells are injected directly into the circulation via i.v. or i.c. delivery. I.v. injection delivers cells into venous circulation and primarily favors lung metastasis, while i.c. injection introduces cells into arterial circulation and supports bone and brain metastasis[13,29,30]. These approaches produce metastasis with more robust, rapid and reproducible kinetics than orthotopic models and enable direct investigation of steps in the metastatic cascade post-intravasation. We investigated whether PDX cells metastasize following i.v. or i.c. delivery after expansion in sphere culture.

We harvested HCI010 and HCI002 tumors from PDX mice and cultured the cells for two weeks in MAT-E conditions (Fig. 5a). 5 $x10^{5}$ P0 sphere cells were injected i.v. or i.c. into

NOD/SCID mice and eight weeks later, peripheral tissues were harvested and analyzed by flow cytometry and histology (Fig. 5a). In i.c. injected animals, we observed human HCI010 MAT-E cells in the lungs (4/5 mice), bone marrow (3/5 mice), brain (5/5 mice) and peripheral blood (5/5 mice), but not the lymph nodes (0/5 mice) (Fig. 5b). Metastatic burden was remarkably robust in the brain, where HCI010 cells constituted >50% of live cells in three of the mice (Fig. 5b). We also observed metastasis in animals injected i.c. with HCI002 cells, where we found human cells in the lungs, brain and peripheral blood (Supplementary Fig. 3a). Like HCI010, metastasis was most robust in the brain, demonstrating the utility of this approach for studies of brain metastasis.

In i.v. injected animals, we observed HCI010 MAT-E cells in the lungs (5/5 mice), bone marrow (1/5 mice), and peripheral blood (1/5 mice), but not the lymph nodes (0/5 mice) (Fig. 5c). As expected, i.v. delivery yielded the highest frequency of metastasis (5/5 mice) (0.96 ± 0.48%) in the lungs (Fig. 5c). Analysis of mice injected i.v. with HCI002 cells showed limited metastasis (Supplementary Fig. 3b). We subsequently tested whether i.v. injection into NSG mice would support greater metastasis of HCI002, since NSG mice displayed more robust metastasis with orthotopic transplants. Indeed, flow cytometry analysis showed 5/5 NSG mice developed lung metastasis, compared to 0/5 NOD/SCID mice (Supplementary Fig. 3b). Histological analysis confirmed the presence of metastatic lesions in the lungs, which showed specific expression of the basal-like marker KRT5 (Fig. 5d, Supplementary Fig. 3c). These data demonstrate that cultured PDX cells are able to metastasize following i.c. and i.v. delivery, and show that expansion in sphere culture facilitates the use of patient tumor cells in experimental metastasis assays.

Validation of PDX culture-transplant system for authentic investigations of metastasis *in vivo*

To investigate whether our approach can be used to study metastasis, we tested whether previously established experimental inhibitors of metastasis have a similar effect on PDX cell metastasis post culture. In prior work, we found that genes associated with mitochondrial oxidative phosphorylation (OXPHOS) are upregulated in spontaneous lung micrometastases from PDX animals using single-cell RNA sequencing (scRNA-seq)[13]. We further showed that inhibition of OXPHOS using Oligomycin (Oligo), a potent inhibitor of mitochondrial complex V, attenuates lung metastasis following i.v. injection of two breast cancer cell lines, 4T1 and MDA-MB-231[13,31]. Here, we determined whether Oligo has a similar effect on the metastatic capacity of our cultured PDX cells following i.v. injection (Fig 6a).

We first evaluated the effects of Oligo on PDX cell viability and metabolism. HCI002 cells were grown for two weeks in MAT-E condition, treated with 1 μM Oligo for three days and monitored for toxicity by microscopy, trypan blue exclusion and aV and PI staining. Spheres were also treated with established cytotoxic agents, including Taxol, doxorubicin (DOX) and staurosporine (STS) for control. Brightfield microscopy revealed no changes in the formation or morphology of PDX spheres following Oligo treatment (Supplementary Fig. 4a). This was in stark contrast to cells treated with cytotoxic agents that caused obvious disintegration of PDX spheres. Trypan blue exclusion analysis showed there was no difference in the percentage of live cells in control (72.3 ± 3.1%) vs. Oligo (72.3 ± 10.2%) treated conditions (Supplementary Fig. 4b). This was confirmed by aV and PI analysis, which showed no significant difference in the percentage of $aV^{-}PI^{-}$ live cells in Oligo (77.8 ± 1.9%) and control (81.0 ± 3.1%) groups (Supplementary Fig. 4c,d).

We next evaluated effects of Oligo on PDX cell metabolism. Oligomycin induces cells to shift from OXPHOS to glycolysis for ATP production[32,33]. We used phasor-based analysis of fluorescence lifetime imaging (FLIM) of NADH to determine whether Oligo induces PDX tumor spheres to shift from OXPHOS to glycolysis. This approach relies on the fact that the

fluorescence lifetime of NADH is longer when bound to enzymes involved in OXPHOS (3.4 ns) than when free floating in the cytoplasm during glycolysis (0.4 ns)[34,35]. HCI002 spheres were treated with Oligo for 6 hours, then wells were washed and replaced with fresh drug-free medium for imaging immediately (0 hours) and 24 hours later (Fig 6b). FLIM showed a 7.4 ± 0.8% increase in the fraction of free NADH at 0 hours, which was sustained and slightly increased at 24 hours (8.9 ± 0.1%) (Fig. 6b). These data confirm that Oligo induces PDX sphere cells to shift from OXPHOS to glycolysis without compromising cell viability.

We injected NSG mice i.v. with 5 x 10^5 sphere cells after 6 hour treatment with Oligo (n=5) or vehicle control (n=6) (Fig 6a). Lungs were harvested lungs 8 weeks later and analyzed by flow cytometry (Fig 6a). Analysis for $CD298^+MHCI^-$ human PDX cells showed a 5.9-fold lower frequency of metastatic cells in the lungs of mice injected with Oligo (0.02 ± 0.01%) compared to vehicle (0.12 ± 0.09%) treated cells (p=0.03) (Fig. 6c). These data show that Oligo substantially attenuates the metastatic capacity of HCI002 PDX cells, and further establish that OXPHOS is critical for lung metastasis. Importantly, our results also agree with prior reports using breast cancer cell lines, validating our PDX culture transplant system for authentic investigations of metastasis using patient cells.

PDX culture-transplant system enables functional interrogation of metastasis-associated genes using patient tumor cells

We used our PDX culture-transplant system to evaluate the role of nucleoside diphosphate kinase A (NME1) in metastasis (Fig. 7a). NME1 catalyzes the transfer of a phosphate from nucleoside triphosphates (NTPs) to nucleoside diphosphates (NDPs), primarily from ATP to GDP to produce GTP for use in G protein signalling[36]. In addition to OXPHOS gene upregulations, we previously found NME1 was upregulated in spontaneous lung micrometastases of HCI010 PDX animals by scRNA-seq (Fig. 7b)[13]. Given the potential link

between OXPHOS-mediated generation of ATP and its use by NME1, we investigated whether NME1 overexpression promotes metastasis using our PDX culture-transplant system.

HCI010 cells were cultured in MAT-E conditions for two weeks (P0) and transduced with lentivirus to overexpress NME1 and GFP (+NME1) or GFP alone (+GFP) (Fig. 7a). Transduced P0 cells were re-plated and expanded in culture for 3 weeks (P1) (Supplementary Fig. 5a). GFP-positive P1 cells were isolated by flow cytometry (Supplementary Fig. 5b), transplanted orthotopically, and animals were analyzed 60 days later. qPCR analysis of sorted +NME1 cells confirmed the ectopic expression of NME1 via lentiviral transduction (Supplementary Fig. 5c). Analysis of primary tumors showed no difference in the mass or growth kinetics of +NME1 (n=6) and +GFP (n=6) groups (Fig. 7c). However, whole mount fluorescence microscopy analysis of lung tissues showed substantially more GFP-positive signal in the +NME1 group, indicating higher metastatic burden (Fig. 7d). This was confirmed by flow cytometry, which showed a >4-fold increase in the frequency of GFP-positive $CD298^{+}MHC\text{-}I^{-}$ human metastatic cells in the lungs of +NME1 (0.98 ± 0.25%) compared to +GFP (0.23 ± 0.15%) control mice (Fig. 7e). These findings reveal a pro-metastatic function for NME1, and provide proof-of-principle for the value of our PDX culture-transplant system for functional investigations of new genes in metastasis with patient tumor cells.

DISCUSSION

A major bottleneck to improving patient outcomes in the setting of metastatic cancer has been the limited number of tools to study this complex biological process. Human cancer cell lines have been utilized in the past[3,4,30], but PDX models provide more biologically relevant methods to studying human cancers[37,38]. Recent work has adapted some transient culture of patient tumor cells for drug screens[8–10], but offer limited opportunities for genetic and/or functional modulation to define crucial mechanisms facilitating metastatic disease. To improve

these tools, we adapted PDX breast cancer models into an *in vitro* and *in vivo* culture-transplant system to functionally study metastasis. We established optimal culture conditions for these PDX tumor cells which favored growth and expansion of viable tumor spheres greater than previously reported methods[8]. These culture conditions maintained cellular identity of PDX cells and their capacity to form primary tumors in mice, which authentically resembled their corresponding native tumors and retained their ability to spontaneously metastasize. Furthermore, we standardized an efficient method for lentiviral transduction and modeled a workflow for functional investigations of new genes in metastasis.

We established i.v. tail vein and i.c. injection models to study post-intravasation metastasis using our cultured PDX cells and functionally demonstrated OXPHOS is crucial for metastasis post-intravasation, corroborating our previous findings[13]. We recently used scRNA-seq and identified mitochondrial OXPHOS as one of the top pathways upregulated in micrometastatic cells compared to primary tumor cells and confirmed these findings with mass spectrometry-generated metabolite profiles with native PDX models[13]. Complementary to these findings, increased mitochondrial biomass, oxygen consumption and OXPHOS has been shown to be associated with metastatic disease[39,40]**.** OXPHOS may offer metastatic cells an advantage because of its ability to generate significant amounts of energy and its versatility; a number of energy sources implicated in metastasis can feed into OXPHOS as intermediates in the Krebs Cycle[41–45].

Having increased levels of cellular ATP generated by OXPHOS could provide an advantage to metastatic cells for dissemination. For example, it may provide a generous source of ATP needed for NME1-mediated G protein activation and its downstream pathways altering cell-cell adhesion, invasion and migration[36]. We previously found NME1 to be increased in expression in HCI010 micrometastatic lung cells compared to primary tumor cells using scRNA-seq[13]. Interestingly, our HCI010 PDX culture-transplant system demonstrated ectopic

expression of NME1 promoted spontaneous metastasis of HCI010 cells to the lungs. In contrast, other reports have demonstrated a suppressive role on metastasis by NME1 in melanoma cells[46–49]. This suggests NME1 may behave differently in a tissue specific context, acting as a suppressor of metastasis in melanoma and a pro-metastatic player in breast cancer. These findings in this technical report demonstrate the utility of our model in defining the role of new metastasis-related genes and warrants follow up studies defining the exact mechanism of NME1-mediated metastasis in the context of breast cancer. Thus, we present a novel PDX culture-transplant system which provides a platform for the functional investigation of metastatic disease using bona fide patient tumor cells.

Materials and Methods

Harvesting and processing tumors into single cells

After 3-6 months of growth, tumors were collected from mice and mechanically dissociated, followed by 2 mg/mL collagenase (Sigma-Aldrich, cat. no. C5138-1G) digestion in medium (DMEM F-12 medium with 5% FBS) at 37°C for 45 minutes on a standard shaker. The digested tumor was washed with PBS, incubated with trypsin (Corning, cat. no. 25-052-Cl) for 10 minutes at 37°C, washed again, and then treated with DNaseI (Worthington Biochemical, cat. no. LS002139). The cells were filtered through a 100 µm strainer. Live cell concentration was checked using the Countess II automated cell counter (ThermoFisher Scientific Inc., Carlsbad, CA, USA).

Culturing PDX cells

PDX tumors were dissociated into single cells and plated in various culture conditions. PDX cells were plated in 6-well ULA plates (Fisher Scientific, cat. no. 07-200-601) at 2.5 x 10^5 cells/well and topped off with 1 mL of either EpiCult™ Medium (StemCell Technologies, cat. no.

05610) supplemented with 5% FBS, 10 ng/mL human epidermal growth factor, and 10 ng/mL basic fibroblast growth factor or MEGM™ culture medium (Lonza, cat. no. CC-3150), completed as per manufacturer's protocol. Medium was changed when necessary.

PDX single cells were also cultured in standard flat bottom 24-well plates. The cells were plated at a seeding density of 1.0 x 10^5 to 2.5 x 10^5 cells/well in a 1:1 mix of Matrigel (growth factor reduced) (Corning, cat. no. 356231) and EpiCult™ or MEGM™. 1 mL of EpiCult medium was added to each well, and changed as necessary. Cells were harvested anytime between day 9-21 using dispase (StemCell Technologies, cat. no. 07913) and trypsin to dissociate Matrigel and spheres. All PDX cells from all culture conditions were grown at 37°C and 5% CO_2.

Generation of bulk RNA-seq data

We generated a dataset of 3 biological replicates of paired HCI010 uncultured and cultured cells, and paired HCI002 uncultured and cultured cells. We harvested and dissociated HCI010 and HCI002 PDX tumors using methods described above. We split our single cell suspension in half and stained half of the uncultured HCI010 and HCI002 cells for FACS using fluorescent labeled antibodies for human specific CD298 (Biolegend, cat. no. 341704) and mouse-specific MHC-I (eBioscience, cat. no. 17-5957-82). 1.0 x10^5 uncultured cells were sorted for each patient for RNA isolation. The other half of the cell suspension was used for culturing. HCI010 and HCI002 PDX cells were plated in 24-well plates at a seeding density of 2.5 x 10^5 cells/well and topped off with 1 mL of EpiCult. Cells were grown in culture for 2 weeks, and then harvested using dispase and trypsin. Cultured cells were stained for FACS using fluorescent labeled antibodies for human-specific CD298 and mouse-specific MHC-I. 1.0 x10^5 cultured cells were sorted for each patient. After sorting, uncultured and cultured cells were processed for RNA extraction, followed by cDNA synthesis and amplification. Library construction was performed with the Takara Clontech SMARTer Stranded Total RNA-seq kit v2. The libraries

were sequenced at a depth of 35 million paired end reads for each sample on the NovaSeq 6000.

Processing and analysis of bulk RNA-seq data

Quality of reads was accessed using FastQC software. Reads were aligned to reference genome GRCh38/hg38 from UCSC using Spliced Transcripts Alignment to a Reference (STAR) software. The un-normalized count matrix was filtered to exclude any genes with 0 reads, and we designated the uncultured samples as the reference level. We then performed differential gene expression analysis using DESeq2 1.28.1 in R 4.0.0.

Mouse strains

NOD/SCID and NSG mice were purchased from The Jackson Laboratory (Bar Harbor, Maine, USA). All mice were maintained in a pathogen-free facility. All mouse procedures were approved by the University of California, Irvine, Institutional Animal Care and Use Committee.

Orthotopic transplantation and i.c and i.v injection models of cultured PDX cells for modeling metastasis

PDX cells were harvested after two to three weeks of culture in Matrigel and EpiCult. Dispase and trypsin were used to dissociate Matrigel and spheres to single cells. For orthotopic transplants, 2.0×10^4 - 1.0×10^5 cells were suspended in 15-20 µL of a 1:1 mixture of PBS and Matrigel and injected into the number 4 mammary fat pads of NOD/SCID and NSG mice using a 25 µL Hamilton syringe. For experimental metastasis models, cells were suspended at a concentration of 5×10^6 cells/mL. 5×10^5 cells in 100ul of PBS were injected into the right ventricle of each NOD/SCID or NSG mouse for i.c. injections or into the tail vein for i.v. injections.

Analysis of primary tumors and metastasis in distal tissues

Following 8-14 weeks post orthotopic transplants, or ~8 weeks post i.c. or i.v. injections, primary tumors and peripheral tissues including lungs, lymph nodes, bone marrow, peripheral blood, and brains were harvested, dissociated to single cells and stained with fluorescent conjugated antibodies for CD298 (Biolegend, cat. no. 341704) and MHC-I (eBioscience, cat. no. 17-5957-82), and flow cytometry was used to analyze and quantify disseminated $CD298^{+}MHC\text{-}I^{-}$ PDX cells using the BD FACSAria Fusion cell sorter (Becton, Dickinson and Company, Franklin Lakes, NJ, USA) as described previously[20]. Primary tumor volumes were calculated using caliper measurements with the equation: volume of an ellipsoid= 1/2(length x $width^2$). Whole mount images of primary tumors and lungs were taken with a Leica MZ10 F modular stereo microscope (Leica Microsystems, Buffalo Grove, IL, USA).

Histology and pathological analysis

Tissues were harvested from mice. The lungs and tumors were fixed in 4% formaldehyde. After overnight fixation at 4°C, the tissues were processed for paraffin embedding using standard protocols. The paraffin-embedded tissues were cut into 7-µm sections using a Leica microtome, rehydrated, and stained with haematoxylin and eosin. For immunofluorescent staining, slides were subjected to antigen retrieval in a 10 mM citric acid buffer (0.05% Tween 20, pH 6.0). We then blocked non-specific binding with a blocking buffer (0.1% Tween 20 and 10% FBS in PBS) for 20 minutes, and then incubated tissues overnight at 4°C with primary antibodies. Slides were washed with PBS, and then incubated at room temperature with secondary antibodies for an hour, followed by washing with PBS, and mounting with VECTASHIELD Antifade Mounting Medium with DAPI (Vector Laboratories, H-1200-10). Images were taken using a BZ-X700 Keyence microscope (Keyonce Corp. of America, Itasca, IL, USA). Pathological analysis was performed by Dr. Robert A. Edwards, a

board-certified pathologist and the director of the Experimental Tissue Resource in the UC Irvine Health Chao Family Comprehensive Cancer Center.

Lentivirus transduction for genetic engineering of PDX cells

PDX cells were cultured for approximately 2-3 weeks in Matrigel and EpiCult, removed from Matrigel with dispase, dissociated to single cells with trypsin, neutralized with DMEM medium with 10% FBS, and washed with PBS with a 5 min centrifugation at 300 x g. Cells were suspended in premade lentivirus solution at a multiplicity of infection (MOI) of 25 and the final volume was topped off to no greater than 100 µL with Opti-MEM™ I Reduced Serum Medium (ThermoFisher Scientific, Cat No. 31985070). GFP control (+GFP) and NME1 (+NME1) lentiviral expression vectors were packaged into lentiviral particles and purchased from VectorBuilder Inc., Chicago, IL, USA (+GFP Cat. No. VB190812-1255tza, +NME1 Cat. No. VB180802-1083ueg). Cells were subjected to an hour long spinfection at 300 x g at 4°C, resuspended and incubated in the same lentivirus solution for an additional 4-5 hours in 96-well round bottom ultra low attachment plate wells at 37°C and 5% CO_2. Cells were centrifuged for 5 min at 300 x g, seeded in Matrigel and EpiCult as described above and expanded for an additional 2-3 weeks at 37°C and 5% CO_2. Medium was replaced as needed. After 2-3 weeks in Matrigel and EpiCult cultured, PDX cells were removed from Matrigel with dispase, dissociated to single cells with trypsin to form single cell suspensions for transplantation into mice. Cell sorting for GFP-positive $CD298^+MHC\text{-}I^-$ PDX cells with fluorescently tagged antibodies for CD298 (Biolegend, cat. no. 341704) and MHC-I (eBioscience, cat. no. 17-5957-82) was performed using the BD FACSAria Fusion cell sorter (Becton, Dickinson and Company, Franklin Lakes, NJ, USA).

Cell death and viability assays

Trypan Blue exclusion assays were performed with the Countess II automated cell counter (ThermoFisher Scientific Inc., Carlsbad, CA, USA). For analysis of cell death, cells were

stained with aV-FITC, diluted 1:100 (GeneTex Cat. No. GTX14082) and PI, diluted 1:100 (ThermoFisher Scientific Cat. No. P3566) for 15 minutes in aV binding buffer (10 mM HEPES, 140 mM NaCl, 2.5 mM $CaCl_2$, pH 7.4). Fluorescence microscopy was performed with the BZ-X700 Keyence microscope (Keyonce Corp. of America, Itasca, IL, USA), and flow cytometry analysis was performed using the BD FACSAria Fusion cell sorter (Becton, Dickinson and Company, Franklin Lakes, NJ, USA).

NADH fluorescence lifetime imaging

NADH fluorescence lifetime images were acquired with an LSM 880 confocal microscope (Zeiss) with a 40x 1.2 NA C-Apochromat water-immersion objective coupled to an A320 FastFLIM acquisition system (ISS). A Ti:Sapphire laser (Spectra-Physics Mai Tai) with an 80 MHz repetition rate was used for two-photon excitation at 740 nm. The excitation signal was separated from the emission signal by a 690 nm dichroic mirror. The NADH signal was passed through a 460/80 nm bandpass filter and collected with an external photomultiplier tube (H7522P-40, Hamamatsu). Cells were imaged within a stage-top incubator kept at 5% CO_2 and 37°C. FLIM data was acquired and analyzed with the SimFCS 4 software developed at the Laboratory for Fluorescence Dynamics at UC Irvine. Calibration of the system was performed by acquiring FLIM images of coumarin 6 (~10 µM), which has a known lifetime of 2.4 ns in ethanol, to account for the instrument response function.

Phasor FLIM NADH fractional analysis

NADH assumes two main physical states, a closed configuration when free in solution, and an open configuration when bound to an enzyme[50]. These two physical states have differing lifetimes, 0.4 ns when in its free configuration, and 3.4 ns when in its bound configuration [51–53]. To quantify metabolic alterations, we performed fractional analysis of NADH lifetime by calculating individual pixel positions on the phasor plot along the linear trajectory of

purely free NADH lifetime (0.4 ns) and purely bound NADH lifetime (3.4 ns). We quantified the fraction of free NADH by calculating the distance of the center of mass of a spheroid's cytoplasmic NADH FLIM pixel distribution to the position of purely bound NADH divided by the distance between purely free NADH and purely bound NADH on the phasor plot. These segmentation and phasor analysis methods are described in detail elsewhere[54].

Single cell analysis

To analyze the differences in the expression of NME1 between metastases and tumors in these models, we accessed our previously published dataset on these PDX models, which included single cell gene expression profiles of metastatic and primary tumor cells[13]. The expression matrices were log-transformed into log[transcripts per kilobase million + 1] matrices and loaded into the Seurat analysis package[55].

qPCR analysis

RNA was extracted by using Quick- RNA Microprep Kit (Zymo Research, R1050) following manufacturer's protocol. RNA concentration and purity were measured with a Pearl nanospectrophotometer (Implen). Quantitative real-time PCR was conducted using PowerUp SYBR green master mix (Thermo Fisher Scientific, A25742) and primer sequences were found in Harvard primer bank and designed from Integrated DNA Technologies; GAPDH forward primer 5'- CTCTCTGCTCCTCCTGTTCGAC -3', GAPDH reverse primer 5'- TGAGCGATGTGGCTCGGCT -3'; NME1 forward primer 5'- AAGGAGATCGGCTTGTGGTTT -3', NME1 reverse primer 5'- CTGAGCACAGCTCGTGTAATC -3'. Gene expression was normalized to the GAPDH housekeeping gene. For relative gene expression 2^neg$\Delta\Delta$Ct values were used. The statistical significance of differences between groups was determined by unpaired t-test using Prism 6 (GraphPad Software, Inc).

Acknowledgements

We thank Dr. Zena Werb at the University of California, San Francisco for thoughtful discussions and feedback on project overview and study design. We thank Armani Oganyan, Nathan Ryan James, Anh Thien Phung, Scott Nguyen, Lannhi Nguyen and Jennifer Nguyen for their technical assistance and animal handling. We thank Dr. Alana Welm at the Huntsman Cancer Institute for generously providing PDX models. We thank the Genomics High Throughput Facility at the University of California, Irvine for conducting the bulk RNA sequencing of the PDX samples. We wish to acknowledge the support of the Chao Family Comprehensive Cancer Center Experimental Tissue Resource, supported by the National Cancer Institute of the National Institutes of Health under award number P30CA062203.

Funding

This study was supported by funds from the National Cancer Institute (K22 CA190511 to D.A.L.), the NIH/NCI (1R01CA234496; 4R00CA181490 to K.K.), the American Cancer Society (132551-RSG-18-194-01-DDC to K.K.), the National Institutes of Health (P41-GM103540 to M.A.D. and A.E.Y.T.L, T32CA009054 to R.T.D through matched university funds), the National Science Foundation (1847005 to M.A.D. and NSF GRFP DGE-1839285 to A.E.Y.T.L) and the V Foundation (V2019-019). H.A. was supported by the University of Hail, Hail, Saudi Arabia for the Ph.D. Fellowship. D.M. was supported by the Canadian Institutes of Health Research Postdoctoral Fellowship.

Competing interests

The authors declare no competing interests.

Author Contributions

D.A.L and K.K. supervised research. D.A.L, K.K., D.M., and G.A.H. designed research. D.M., G.A.H., A.E.Y.T.L., H.A., K.B., K.R.D., M.R., J.W.W., R.T.D, K.T.E., M.Y.G.M., R.L., R.A.E., M.A.D., K.K., and D.A.L. performed research; G.A.H., K.B., and J.W.W. performed bioinformatic analyses; D.M., G.A.H., K.K. and D.A.L. wrote the paper manuscript, and all authors discussed the results and provided comments and feedback.

Data availability

The authors declare that all data supporting the findings of this study are available within the article and its supplementary information files or from the corresponding author upon reasonable request.

References

1. DeSantis, C. E. *et al.* Breast cancer statistics, 2015: Convergence of incidence rates between black and white women. *CA. Cancer J. Clin.* **66**, 31–42 (2016).

2. Lambert, A. W., Pattabiraman, D. R. & Weinberg, R. A. Emerging Biological Principles of Metastasis. *Cell* **168**, 670–691 (2017).

3. Frese, K. K. & Tuveson, D. A. Maximizing mouse cancer models. *Nat. Rev. Cancer* **7**, 654–658 (2007).

4. Neve, R. M. *et al.* A collection of breast cancer cell lines for the study of functionally distinct cancer subtypes. *Cancer Cell* **10**, 515–27 (2006).

5. DeRose, Y. S. *et al.* Tumor grafts derived from women with breast cancer authentically reflect tumor pathology, growth, metastasis and disease outcomes. *Nat. Med.* **17**, 1514–

1520 (2011).

6. Hidalgo, M. *et al.* Patient-derived xenograft models: an emerging platform for translational cancer research. *Cancer Discov.* **4**, 998–1013 (2014).

7. Tentler, J. J. *et al.* Patient-derived tumour xenografts as models for oncology drug development. *Nat. Rev. Clin. Oncol.* **9**, 338–350 (2012).

8. Bruna, A. *et al.* A Biobank of Breast Cancer Explants with Preserved Intra-tumor Heterogeneity to Screen Anticancer Compounds. *Cell* **167**, 260-274.e22 (2016).

9. DeRose, Y. S. *et al.* Patient-Derived Models of Human Breast Cancer: Protocols for In Vitro and In Vivo Applications in Tumor Biology and Translational Medicine. *Curr. Protoc. Pharmacol.* **60**, Unit14.23 (2013).

10. Sachs, N. *et al.* A Living Biobank of Breast Cancer Organoids Captures Disease Heterogeneity. *Cell* **172**, 373-386.e10 (2018).

11. Lee, G. Y., Kenny, P. A., Lee, E. H. & Bissell, M. J. Three-dimensional culture models of normal and malignant breast epithelial cells. *Nat. Methods* **4**, 359–65 (2007).

12. Shafee, N. *et al.* Cancer Stem Cells Contribute to Cisplatin Resistance in Brca1/p53–Mediated Mouse Mammary Tumors. *Cancer Res.* **68**, 3243 (2008).

13. Davis, R. T. *et al.* Transcriptional diversity and bioenergetic shift in human breast cancer metastasis revealed by single-cell RNA sequencing. *Nat. Cell Biol.* **22**, 310–320 (2020).

14. Byun, Y.-S. *et al.* Keratocytes Derived from Spheroid Culture of Corneal Stromal Cells Resemble Tissue Resident Keratocytes. *PLoS One* **9**, (2014).

15. Yu, M. *et al.* Ex vivo culture of circulating breast tumor cells for individualized testing of

drug susceptibility. *Science* **345**, 216 (2014).

16. Edmondson, R., Broglie, J. J., Adcock, A. F. & Yang, L. Three-Dimensional Cell Culture Systems and Their Applications in Drug Discovery and Cell-Based Biosensors. *Assay Drug Dev. Technol.* **12**, 207 (2014).

17. N, S. *et al.* Cancer Stem Cells Contribute to Cisplatin Resistance in Brca1/p53-mediated Mouse Mammary Tumors. *Cancer Res.* **68**, (2008).

18. Shimono, Y. *et al.* Downregulation of miRNA-200c Links Breast Cancer Stem Cells with Normal Stem Cells. *Cell* **138**, 592–603 (2009).

19. Vermes, I., Haanen, C. & Reutelingsperger, C. Flow cytometry of apoptotic cell death. *J. Immunol. Methods* **243**, 167–190 (2000).

20. Lawson, D. A. *et al.* Single-cell analysis reveals a stem-cell program in human metastatic breast cancer cells. *Nature* **526**, 131–5 (2015).

21. Love, M. I., Huber, W. & Anders, S. Moderated estimation of fold change and dispersion for RNA-seq data with DESeq2. *Genome Biol.* **15**, 550 (2014).

22. Yoneda, J. *et al.* Expression of Angiogenesis-Related Genes and Progression of Human Ovarian Carcinomas in Nude Mice. *JNCI J. Natl. Cancer Inst.* **90**, 447–454 (1998).

23. Kim, S. J. *et al.* Expression of interleukin-8 correlates with angiogenesis, tumorigenicity, and metastasis of human prostate cancer cells implanted orthotopically in nude mice. *Neoplasia* **3**, 33–42 (2001).

24. Vandercappellen, J., Van Damme, J. & Struyf, S. The role of CXC chemokines and their receptors in cancer. *Cancer Lett.* **267**, 226–244 (2008).

25. Keeley, E. C., Mehrad, B. & Strieter, R. M. Chemokines as mediators of tumor angiogenesis and neovascularization. *Exp. Cell Res.* **317**, 685–90 (2011).

26. Kleinman, H. K. & Martin, G. R. Matrigel: Basement membrane matrix with biological activity. *Semin. Cancer Biol.* **15**, 378–386 (2005).

27. DeRose, Y. S. *et al.* Tumor grafts derived from women with breast cancer authentically reflect tumor pathology, growth, metastasis and disease outcomes. *Nat. Med.* **17**, 1514–20 (2011).

28. López-Soto, A., Gonzalez, S., Smyth, M. J. & Galluzzi, L. Control of Metastasis by NK Cells. *Cancer Cell* **32**, 135–154 (2017).

29. Bos, P. D. *et al.* Genes that mediate breast cancer metastasis to the brain. *Nature* **459**, 1005–1009 (2009).

30. Richert, M. M. *et al.* Metastasis of hormone-independent breast cancer to lung and bone is decreased by α-difluoromethylornithine treatment. *Breast Cancer Res.* **7**, R819 (2005).

31. Symersky, J., Osowski, D., Walters, D. E. & Mueller, D. M. Oligomycin frames a common drug-binding site in the ATP synthase. *Proc. Natl. Acad. Sci. U. S. A.* **109**, 13961 (2012).

32. Hao, W., Chang, C.-P. B., Tsao, C.-C. & Xu, J. Oligomycin-induced Bioenergetic Adaptation in Cancer Cells with Heterogeneous Bioenergetic Organization. *J. Biol. Chem.* **285**, 12647–12654 (2010).

33. Choi, S. W., Gerencser, A. A. & Nicholls, D. G. Bioenergetic Analysis of Isolated Cerebrocortical Nerve Terminals on a Microgram Scale: Spare Respiratory Capacity and Stochastic Mitochondrial Failure. *J. Neurochem.* **109**, 1179 (2009).

34. Chance, B. Mitochondrial NADH Redox State, Monitoring Discovery and Deployment in Tissue. *Methods Enzymol.* **385**, 361–370 (2004).

35. Stringari, C., Nourse, J. L., Flanagan, L. A. & Gratton, E. Phasor Fluorescence Lifetime Microscopy of Free and Protein-Bound NADH Reveals Neural Stem Cell Differentiation Potential. *PLoS One* **7**, e48014 (2012).

36. Boissan, M., Schlattner, U. & Lacombe, M.-L. The NDPK/NME superfamily: state of the art. *Lab. Investig.* **98**, 164–174 (2018).

37. Daniel, V. C. *et al.* A Primary Xenograft Model of Small-Cell Lung Cancer Reveals Irreversible Changes in Gene Expression Imposed by Culture In vitro. *Cancer Res.* **69**, 3364–3373 (2009).

38. Whittle, J. R., Lewis, M. T., Lindeman, G. J. & Visvader, J. E. Patient-derived xenograft models of breast cancer and their predictive power. *Breast Cancer Res.* **17**, 17 (2015).

39. Andrzejewski, S. *et al.* PGC-1α Promotes Breast Cancer Metastasis and Confers Bioenergetic Flexibility against Metabolic Drugs. *Cell Metab.* **26**, 778-787.e5 (2017).

40. LeBleu, V. S. *et al.* PGC-1α mediates mitochondrial biogenesis and oxidative phosphorylation in cancer cells to promote metastasis. *Nat Cell Biol* **16**, 1-15,992-1003 (2014).

41. Camarda, R. *et al.* Inhibition of fatty acid oxidation as a therapy for MYC-overexpressing triple-negative breast cancer. *Nat. Med.* **22**, 427–32 (2016).

42. Christen, S. *et al.* Breast Cancer-Derived Lung Metastases Show Increased Pyruvate Carboxylase-Dependent Anaplerosis. *Cell Rep.* **17**, 837–848 (2016).

43. Dornier, E. *et al.* Glutaminolysis drives membrane trafficking to promote invasiveness of breast cancer cells. *Nat. Commun.* **8**, 2255 (2017).

44. Elia, I. *et al.* Proline metabolism supports metastasis formation and could be inhibited to selectively target metastasizing cancer cells. *Nat. Commun.* **8**, 15267 (2017).

45. Yang, L. *et al.* Metabolic shifts toward glutamine regulate tumor growth, invasion and bioenergetics in ovarian cancer. *Mol. Syst. Biol.* **10**, 728 (2014).

46. MacDonald, N. ., la Rosa, D. & Steeg, P. . The potential roles of nm23 in cancer metastasis and cellular differentiation. *Eur. J. Cancer* **31**, 1096–1100 (1995).

47. Zhang, Q., McCorkle, J. R., Novak, M., Yang, M. & Kaetzel, D. M. Metastasis suppressor function of NM23-H1 requires its 3′-5′ exonuclease activity. *Int. J. Cancer* **128**, 40–50 (2011).

48. Prasad, V. V. & Gopalan, R. O. Continued use of MDA-MB-435, a melanoma cell line, as a model for human breast cancer, even in year, 2014. *npj Breast Cancer* **1**, 15002 (2015).

49. Jarrett, S. G. *et al.* NM23 deficiency promotes metastasis in a UV radiation-induced mouse model of human melanoma. *Clin. Exp. Metastasis* **30**, 25–36 (2013).

50. Hull, R. V., Conger, P. S. & Hoobler, R. J. Conformation of NADH studied by fluorescence excitation transfer spectroscopy. *Biophys. Chem.* **90**, 9–16 (2001).

51. Kolb, D. A. & Weber, G. Quantitative demonstration of the reciprocity of ligand effects in the ternary complex of chicken heart lactate dehydrogenase with nicotinamide adenine dinucleotide and oxalate. *Biochemistry* **14**, 4471–4476 (1975).

52. Ma, N., Digman, M. A., Malacrida, L. & Gratton, E. Measurements of absolute

concentrations of NADH in cells using the phasor FLIM method. *Biomed. Opt. Express* **7**, 2441 (2016).

53. Datta, R., Alfonso-García, A., Cinco, R. & Gratton, E. Fluorescence lifetime imaging of endogenous biomarker of oxidative stress. *Sci. Rep.* **5**, 9848 (2015).

54. Ranjit, S., Malacrida, L., Jameson, D. M. & Gratton, E. Fit-free analysis of fluorescence lifetime imaging data using the phasor approach. *Nat. Protoc.* **13**, 1979–2004 (2018).

55. Butler, A., Hoffman, P., Smibert, P., Papalexi, E. & Satija, R. Integrating single-cell transcriptomic data across different conditions, technologies, and species. *Nat. Biotechnol.* **36**, 411–420 (2018).

Figure Legends

Figure 1. Comparison of 3D culture methods for viable propagation of PDX tumor cells *in vitro*

(a) Schematic of culture conditions screened for viable maintenance of PDX cells in vitro.

(b) Representative brightfield images of HCI010 cells at 7-14 days after plating 2.5 x 10^5 cells in each condition. Scale bars = 300 µm (top row), 100 µm (bottom row).

(c) Bar graph shows percent of viable HCI010 cells by trypan blue exclusion (one-way ANOVA: *p<0.0001, n=3-6 wells/condition). Data represented as mean ± s.d. Unpaired t-tests: p<0.0001 ULA-E vs MAT-E and ULA-E vs MAT-M; p=0.0004 ULA-E vs ULA-M.

(d) Bar graph shows percent of live and dead HCI010 cells by aV and PI. Data represented as mean ± s.d. (two-way ANOVA: *p<0.0001, n=3 per condition). Unpaired t-tests, aV^-PI^- viable cells: p<0.0001 MAT-E vs MAT-M, MAT-E vs ULA-E, and MAT-E vs ULA-M.

(e) Bar graph quantifies HCI010 cell expansion. Cells were plated at 1.0 x 10^5 cells/well (dashed line), and quantified 9 days later by trypan blue exclusion (one-way ANOVA: *p<0.0001, n=5-11 wells per condition). Data represented as mean ± s.d. Unpaired t-tests: p=0.0162 MAT-E vs MAT-M; p=0.0138 MAT-E vs ULA-E; p<0.0001 MAT-E vs ULA-M.

(f) Schematic overview comparing capacity of MAT-E and MAT-M to support passaging and expansion. HCI010 cells were cultured for 2 weeks, dissociated, and re-plated at 5.0 x 10^4 cells/well (n=3 wells/condition) in MAT-E and MAT-M.

(g) Bar graph shows percentage of viable HCI010 cells by trypan blue exclusion (unpaired t-test: *p=0.004, n=3). Data represented as mean ± s.d.

(h) Bar graph shows percent of live and dead cell populations in MAT-E and MAT-M determined by aV and PI (unpaired t-test: p<0.0001 aV^-PI^- viable cells, n=3)**.** Data represented as mean ± s.d.

(i) Bar graph quantifies HCI010 cell expansion. Cells were plated at 5.0 x 10^4 cells/well (dashed line), and live cells were quantified 21 days later by trypan blue exclusion (unpaired t-test: p=0.008, n=3). Data represented as mean ± s.d.

Figure 2. PDX tumor sphere cells maintain cellular identity and authenticity *in vitro*

(a) Workflow schematic for generation of bulk RNA sequencing data.

(b) Correlation scatter plots of cultured and uncultured differential gene expression for HCI010 (top row) and HCI002 (bottom row). Pearson's correlation coefficient (R^2) shown for each matched uncultured and cultured pair.

(b) Volcano plot showing genes significantly ($p<0.05$) upregulated with a log2FoldChange>2 in cultured cells (n=277, pink dots) with top 8 genes labeled, and genes significantly ($p<0.05$) downregulated with a log2FoldChange<-2 (n=1455, green dots).

(c) Plot showing significant ($p<0.05$) Gene Ontology (GO) terms associated with differentially expressed genes in cultured cells. P-value determined by Fisher's exact test.

(d) Bar graph showing log2FoldChange of significant ($p<0.05$) upregulated genes in cultured cells associated with selected GO terms.

Figure 3. PDX tumor sphere cells maintain tumorigenic potential and form spontaneous metastasis *in vivo*

(a) Schematic overview of workflow and timeline for assessing the capacity of cultured PDX cells to generate primary tumors and spontaneous metastasis following orthotopic transplantation.

(b) Table (top) showing the frequency of tumors generated in serial dilution transplantation study, where HCI010 cells cultured in MAT-E condition were injected orthotopically into NOD/SCID mice. (Bottom) Representative image of primary tumors from orthotopic transplantation of 1×10^5 cultured HCI010 MAT-E cells after 8 weeks of growth. Scale bar = 1cm.

(c) Histopathological and molecular marker analysis of tumors generated from native uncultured (HCI010) and cultured (HCI010 MAT-E) cells. Top panels show representative histopathological

appearance of tumor sections stained with hematoxylin and eosin (H&E). Scale bar= 50 µm. Middle and bottom panels show representative images of IF staining for basal (KRT5), luminal (KRT18) and myoepithelial (SMA) cell markers. Scale bar= 50 µm.

(d) Quantification of spontaneous metastasis in animals transplanted with cultured HCI010 cells. Representative plots (top) show quantification of $CD298^{+}MHC\text{-}I^{-}$ human metastatic PDX cells in distal tissues by flow cytometry. Bar graph (bottom) shows quantification of frequency of metastatic cells in a cohort of transplanted animals. Fractions indicate the number of tissues with metastasis, defined by >0.005% $CD298^{+}MHC\text{-}I^{-}$ cells. Data is represented as the mean ± s.d.

(e) Representative images of metastatic lesions in the lungs of animals transplanted with cultured HCI010 cells identified by H&E staining. Scale bar= 50 µm.

Figure 4. PDX tumor sphere cells can be genetically engineered for functional studies of metastasis *in vivo*

(a) Workflow incorporating transduction protocol of PDX cells to study a gene of interest and its potential role in metastasis.

(b) Representative Z-stack micrographs of an entire well of HCI010 MAT-E cells 1 week post transduction (+GFP, MOI=25) and seeding 2 x 10^5 cells in MAT-E culture (P1) taken with a 2X objective lens. Scale bar= 800 µm.

(c) Representative PDX spheroids 2 weeks post transduction (+GFP, MOI=25) and expansion in MAT-E culture (P1) taken with a 10X objective. Scale bar= 50 µm.

(d) Representative flow cytometry plots for transduction efficiency of PDX cells 2 weeks post transduction (+GFP, MOI=25) and MAT-E culture (P1). Bar graph is a quantitative summary of the number of PDX cells positive for GFP 2 weeks post transduction and culture. Values are represented as the mean ± s.d. (n= 3).

(e) Representative light and fluorescence whole mount micrographs of PDX tumors produced 60 days post orthotopic transplantation of 1 x 10^5 FACS purified transduced PDX cells into NSG mice. Scale bar= 5 mm.

(f) Representative flow cytometry plots quantifying GFP positive cells from PDX tumors produced 60 days post orthotopic transplantation of 1 x 10^5 FACS purified transduced PDX cells (+GFP, MOI=25) into NSG mice. Bar graph is a quantitative summary of the number of tumor cells positive for GFP. Values are represented as the mean ± s.d. (n= 5).

(g) Representative fluorescence micrographs of GFP positive HCI010 MAT-E and HCI002 MAT-E metastatic tumors in the lungs 60 days post orthotopic transplantation of 1 x 10^5 FACS purified transduced PDX cells into NSG mice. Dashed red outline highlights perimeter of metastatic lesions. Scale bar= 50 µm.

(h) Representative flow cytometry plots quantifying GFP positive cells from PDX metastatic lung cells produced 60 days post orthotopic transplantation of 1 x 10^5 FACS purified transduced PDX cells into NSG mice. Bar graph is a quantitative summary of the number of PDX cells positive for GFP. Values are represented as the mean ± s.d. (n= 5).

Figure 5. PDX tumor sphere cells produce robust experimental metastasis *in vivo*

(a) Workflow of i.c. and i.v. models of metastasis with cultured PDX cells.

(b) Representative flow cytometry dot plots showing CD298^{+}MHC-I^{-} human metastatic cells in lungs, lymph nodes, bone marrow, brain, and blood 8 weeks following i.c. injection of 5 x 10^{5} HCI010 MAT-E cells. Bar graph provides a quantitative summary of metastatic frequencies of CD298^{+}MHC-I^{-} HCI010 MAT-E cells in peripheral tissues produced from i.c. injections. Data is represented as the mean ± s.d. (n= 5). Fraction of mice with metastasis at each peripheral tissue was determined using a threshold of 0.005% PDX cells out of all live cells.

(c) Representative flow cytometry plots showing CD298^{+}MHC-I^{-} human metastatic cells in peripheral tissues 8 weeks following i.v. injection of 5 x 10^{5} HCI-010 MAT-E cells in NOD/SCID mice. Bar graph provides a quantitative summary of metastatic frequencies of CD298^{+}MHC-I^{-} PDX cells in peripheral tissues. Data is represented as the mean ± s.d. (n= 5). Fraction of mice with metastasis at each peripheral tissue was determined using a threshold of 0.005% PDX cells out of all live cells.

(d) Representative H & E micrographs of metastatic lesions in the lungs 8 weeks following i.v. injection of 5 x 10^{5} HCI010 MAT-E cells. Arrows indicate metastatic lesions. Scale bar = 50 µm.

(e) Representative immunofluorescence micrographs of metastatic lesions in the lungs 8 weeks following i.v. injection of 5 x 10^{5} HCI010 MAT-E cells. Arrows indicate metastatic lesions. Scale bar = 50 µm.

Figure 6. Validation of PDX culture-transplant system for authentic investigations of metastasis *in vivo*

(a) Schematic of experimental workflow.

(b) (Top panel) Experimental NADH FLIM workflow. (Bottom panel) Representative FLIM images of HCI002 spheroids after 6 hours of treatment with 1 µM Oligo and replacement with fresh medium (time= 0 hours) and 24 hours post medium change. Scale bar= 20 µm. (Right panel) Quantification of the unbound NADH fraction for the FLIM images at times 0 and 24 hours. Values are normalized to the free NADH fraction in control cells at each time point for each replicate, such that a value of 1 represents no change in free NADH compared to control. Values are presented as the mean ± s.d.; control n= 47 spheres at time t= 0 and 24 hours, Oligo n= 46 at time t= 0 and 24 hours. Unpaired t-test: *p< 0.0001. Homoscedasticity determined via F-test.

(c) Representative flow cytometry plots identifying the number of human $CD298^{+}MHC\text{-}I^{-}$ HCI002 MAT-E cells metastasized to the lungs eight weeks post i.v. tail vein injections. Bar graph is a summary of the frequencies of metastatic cells found in the lungs. Values are expressed as mean ± s.d.; control n= 5, Oligo n= 6. Unpaired t-test: *p= 0.0288.

Figure 7. PDX culture-transplant system enables functional interrogation of metastasis-associated genes using patient tumor cells

(a) Schematic of experimental workflow.

(b) Box plots visualizing the normalized gene expression of NME1 in metastatic (red, n = 435 cells) or primary tumour cells (blue, n = 684 cells). The lower and upper hinges correspond to the first and third quartiles, and the midline represents the median. The upper and lower whiskers extend from the hinge up to 1.5 * IQR (inter-quartile range). Outlier points are indicated if they extend beyond this range.

(c) Volumes of primary tumors from orthotopic transplants of 2 x 10^4 transduced +NME1 and +GFP HCI010 MAT-E cells into NSG mice were monitored over a 60 day period with calipers.

Tumor masses were measured after dissection at day 60. Endpoint tumor volumes and masses at 60 days were not significantly different between groups (+GFP n=6, +NME1 n=6); tumor volume p=0.4667; tumor mass p=0.4689. Values are expressed as mean ± s.d.

(d) Representative light and fluorescence whole mount images of lungs from mice orthotopically transplanted with 2 x 10^4 +GFP or +NME1 transduced HCI010 cells. Metastatic lesions appear as GFP-positive fluorescent punctate nodules. Scale bar= 5 mm.

(e) Representative flow cytometry plots quantifying the percentage of human $CD298^+MHC\text{-}I^-$ HCI010 MAT-E cells metastasized to the lungs 60 days post orthotopic transplantation (top) and the percentage of metastatic cells positive for GFP (bottom). Bar graph summarizes the frequencies of metastatic cells found in the lungs. Values are expressed as mean ± s.d.; +GFP n= 6, +NME1 n= 6. Unpaired t-test: $*p < 0.0001$.

Supplementary Figure Legends

Supplementary Figure 1: Evaluation of PDX cell culture conditions

(a) Representative flow cytometry plots of annexin V and PI dead cell analysis of HCI010 cells after two weeks in four culture conditions: MAT-E, MAT-M, ULA-E, or ULA-M.

(b) Representative brightfield images at day 1, 7, and 14 of HCI010 PDX cells grown in MAT-E. Scale bar= 100 µm.

(c) Representative brightfield images of PDX spheres grown in MAT-E culture conditions. Scale bar= 100 µm.

(d) Flow cytometry analysis of human and mouse cells from PDX cell culture, as defined by the markers CD298 and MHCI.

Supplementary Figure 2: Analysis of primary tumors and spontaneous metastases generated via orthotopic transplantation of cultured PDX cells

(a) Table (top) showing the frequency of tumors generated in serial dilution transplantation study, where HCI002 cells cultured in MAT-E conditions were injected orthotopically into NOD/SCID mice. (Bottom) Representative images of tumors generated from orthotopic transplantation of 1 x 10^5 HCI002 MAT-E cells after 12 weeks of growth. Scale bar= 1 cm.

(b) Representative H&E stained sections of tumors generated from native uncultured (HCI002) and cultured (HCI002 MAT-E) cells in NOD/SCID mice. Scale bar= 50 µm.

(c) Comparison of lung metastatic burden in NOD/SCID and NSG animals transplanted orthotopically with 1x10^5 cultured HCI010 cells. Representative plots show quantification of CD298$^+$MHC-I$^-$ human metastatic PDX cells in the lungs 8 weeks after transplant by flow cytometry. Bar graph shows quantification of frequency of metastatic cells in a cohort of transplanted animals (unpaired t-test: p=0.0001, n=11 NOD/SCID, n=5 NSG). Data is represented as the mean ± s.d. Fractions indicate the number of tissues with metastasis, defined by >0.005% CD298$^+$MHC-I$^-$ cells.

(d) Quantification of spontaneous lung metastasis in NSG mice transplanted with 1 x 10^5 MAT-E cultured HCI002 cells. Representative plots show quantification of CD298$^+$MHC-I$^-$ human metastatic PDX cells in the lung by flow cytometry. Bar graph shows quantification of frequency of metastatic cells in a cohort of transplanted animals (n=5). Fractions indicate the number of tissues with metastasis, defined by >0.005% CD298$^+$MHC-I$^-$ cells. Data is represented as the mean ± s.d.

(e) Representative images of metastatic lesions in the lungs of animals transplanted with cultured HCI002 cells identified by H&E staining. Scale bar= 50 µm.

Supplementary Figure 3: PDX tumor sphere cells produce robust experimental metastasis *in vivo*

(a) Representative flow cytometry plots showing $CD298^{+}MHC\text{-}I^{-}$ human metastatic cells in lungs, lymph nodes, bone marrow, brain, and blood 8 weeks following i.c. injection of 5 x 10^5 HCI002 MAT-E cells into NOD/SCID mice.

(b) Representative flow cytometry plots showing $CD298^{+}MHC\text{-}I^{-}$ human metastatic cells in lungs 8 weeks following i.v. injection of 5 x 10^5 HCI002 MAT-E cells in NOD/SCID and NSG mice. Fraction of mice with metastasis was determined using a threshold of 0.005% PDX cells out of all live cells. Bar graph provides a quantitative summary of metastatic frequencies of $CD298^{+}MHC\text{-}I^{-}$ PDX cells. Data is represented as the mean ± s.d. (n= 5). Unpaired t-test: *p=0.0232.

(c) Representative H & E and immunofluorescence micrographs of metastatic lesions in the lungs 8 weeks following i.v. injection of 5 x 10^5 HCI002 MAT-E cells into NSG mice. Arrows indicate metastatic lesions. Scale bar = 50 µm.

Supplementary Figure 4: Cytotoxicity and cell death analysis of PDX cells post drug treatment.

(a) Z-stack brightfield images of representative HCI002 MAT-E spheroids grown for two weeks and treated with the indicated drugs for 72 hours. Scale bar= 50 µm. Oligo= oligomycin; DOX= doxorubicin; STS= staurosporine.

(b) Trypan blue exclusion viability assay of HCI002 MAT-E cells grown for two weeks and treated with the indicated drugs for 72 hours. Values expressed as mean ± s.d. from triplicate wells (n=3). Unpaired t-tests: *p<0.0001 Taxol and STS vs. Control; *p= 0.0002 DOX vs. Control.

(c) Representative flow cytometry plots of aV and PI dead cell analysis of HCI002 MAT-E cells treated for 72 hours. Bar graph shows percent of live and dead HCI002 cells by aV and PI. Data represented as mean ± s.d. (n=3). Unpaired t-tests, $aV^{-}PI^{-}$ viable cells: *p<0.0001 vs. Control. Taxol, DOX and STS were used as positive controls for cell death.

(d) Representative aV and PI fluorescence micrographs of HCI002 MAT-E cells treated for 72 hours. Blue= Hoechst nuclear counterstain. Scale bar= 25 µm.

Supplementary Figure 5: PDX culture-transplant system enables functional interrogation of metastasis-associated genes using patient tumor cells

(a) Representative Z-stack micrographs of an entire well of HCI010 cells 3 weeks post transduction (+NME1, MOI=25) and seeding HCI010 2 x 10^5 cells in MAT-E culture (P1) taken with a 2X objective lens. Scale bar= 800 µm.

(b) Flow cytometry gating strategy for sorting +NME1 transduced cells for orthotopic transplantation in mice and qPCR analysis.

(c) qPCR analysis confirmation of NME1 expression in +NME1 transduced cells. Values are expressed as fold change in expression relative to +GFP cells and represented as mean ± s.d.; +GFP n= 3, +NME1 n= 3. Unpaired t-test: *p= 0.0005 vs. +GFP.

Supplementary Videos 1-3: Growth of HCI010 cells in MAT-E

Time-lapse imaging of HCI010 PDX cells in MAT-E at day 7 of culture. Growth shown over the course of 48 hours.

Figure 1

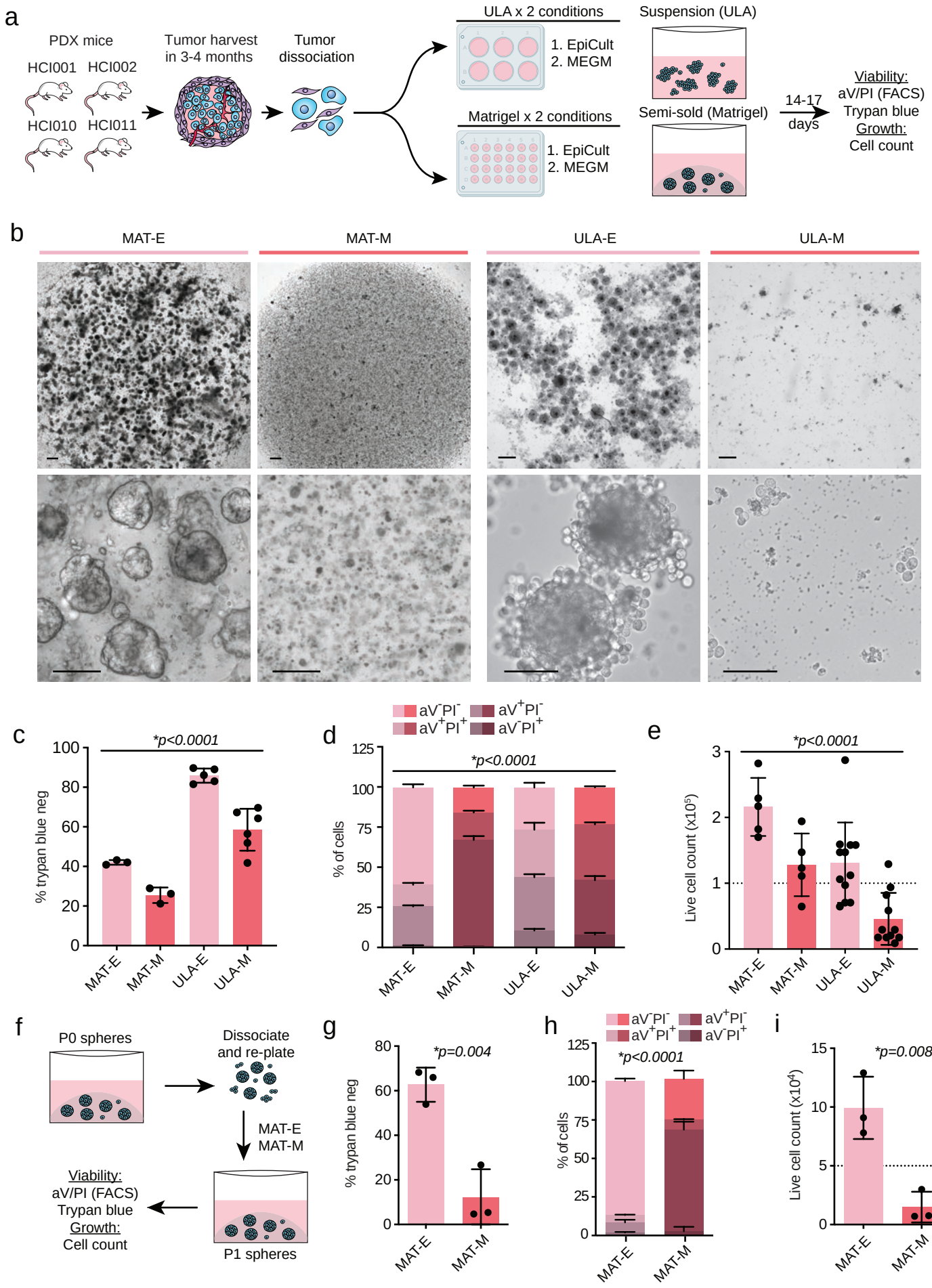
a
PDX mice
HCI001
HCI002
HCI010
HCI011
Tumor harvest in 3-4 months
Tumor dissociation
ULA x 2 conditions
1. EpiCult
2. MEGM
Matrigel x 2 conditions
1. EpiCult
2. MEGM
Suspension (ULA)
Semi-sold (Matrigel)
14-17 days
Viability:
aV/PI (FACS)
Trypan blue
Growth:
Cell count
b
MAT-E
MAT-M
ULA-E
ULA-M
c
*p<0.0001
% trypan blue neg
MAT-E
MAT-M
ULA-E
ULA-M
d
aV-PI-
aV+PI-
aV+PI+
aV-PI+
*p<0.0001
% of cells
e
*p<0.0001
Live cell count (x10^5)
f
P0 spheres
Dissociate and re-plate
MAT-E
MAT-M
P1 spheres
Viability:
aV/PI (FACS)
Trypan blue
Growth:
Cell count
g
*p=0.004
% trypan blue neg
h
*p<0.0001
% of cells
i
*p=0.008
Live cell count (x10^4)

Figure 2

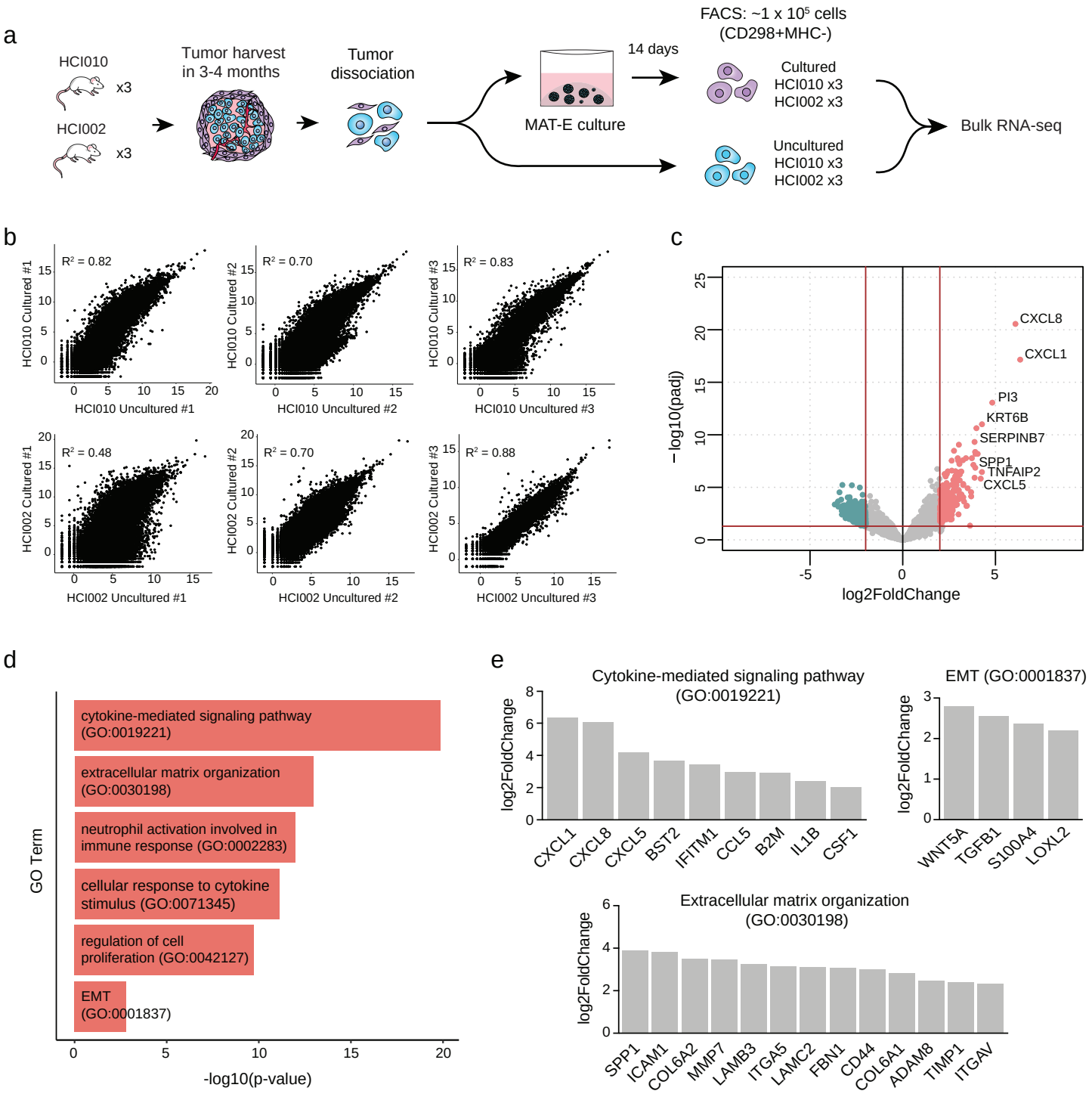
a
HCI010
x3
HCI002
x3
Tumor harvest in 3-4 months
Tumor dissociation
MAT-E culture
14 days
FACS: ~1 x 10⁵ cells (CD298+MHC-)
Cultured HCI010 x3 HCI002 x3
Uncultured HCI010 x3 HCI002 x3
Bulk RNA-seq
b
R² = 0.82
HCI010 Cultured #1
HCI010 Uncultured #1
R² = 0.70
HCI010 Cultured #2
HCI010 Uncultured #2
R² = 0.83
HCI010 Cultured #3
HCI010 Uncultured #3
R² = 0.48
HCI002 Cultured #1
HCI002 Uncultured #1
R² = 0.70
HCI002 Cultured #2
HCI002 Uncultured #2
R² = 0.88
HCI002 Cultured #3
HCI002 Uncultured #3
c
CXCL8
CXCL1
PI3
KRT6B
SERPINB7
SPP1
TNFAIP2
CXCL5
−log10(padj)
log2FoldChange
d
cytokine-mediated signaling pathway (GO:0019221)
extracellular matrix organization (GO:0030198)
neutrophil activation involved in immune response (GO:0002283)
cellular response to cytokine stimulus (GO:0071345)
regulation of cell proliferation (GO:0042127)
EMT (GO:0001837)
GO Term
-log10(p-value)
e
Cytokine-mediated signaling pathway (GO:0019221)
log2FoldChange
CXCL1
CXCL8
CXCL5
BST2
IFITM1
CCL5
B2M
IL1B
CSF1
EMT (GO:0001837)
WNT5A
TGFB1
S100A4
LOXL2
Extracellular matrix organization (GO:0030198)
SPP1
ICAM1
COL6A2
MMP7
LAMB3
ITGA5
LAMC2
FBN1
CD44
COL6A1
ADAM8
TIMP1
ITGAV

Figure 3

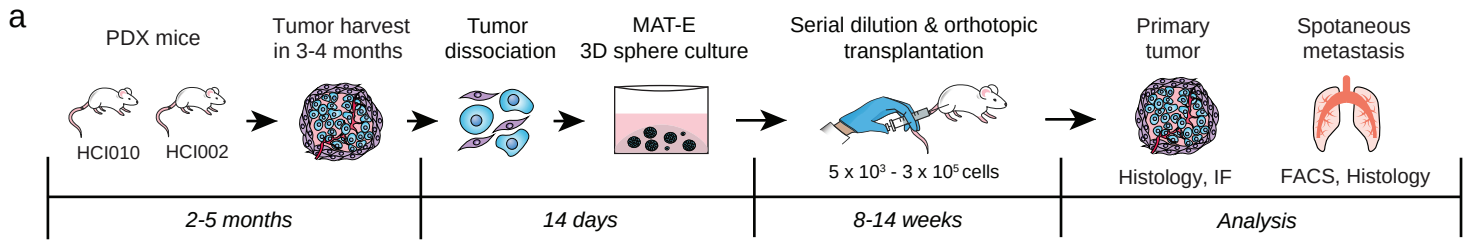

b

PDX model	Cell number	Tumor frequency
HCI010 MAT-E	5.0×10^3	5/5
HCI010 MAT-E	1.0×10^4	10/10
HCI010 MAT-E	1.0×10^5	15/15
HCI010 MAT-E	3.0×10^5	10/10

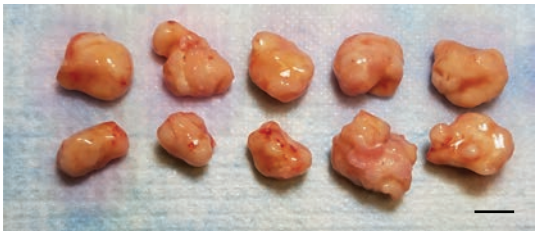

c

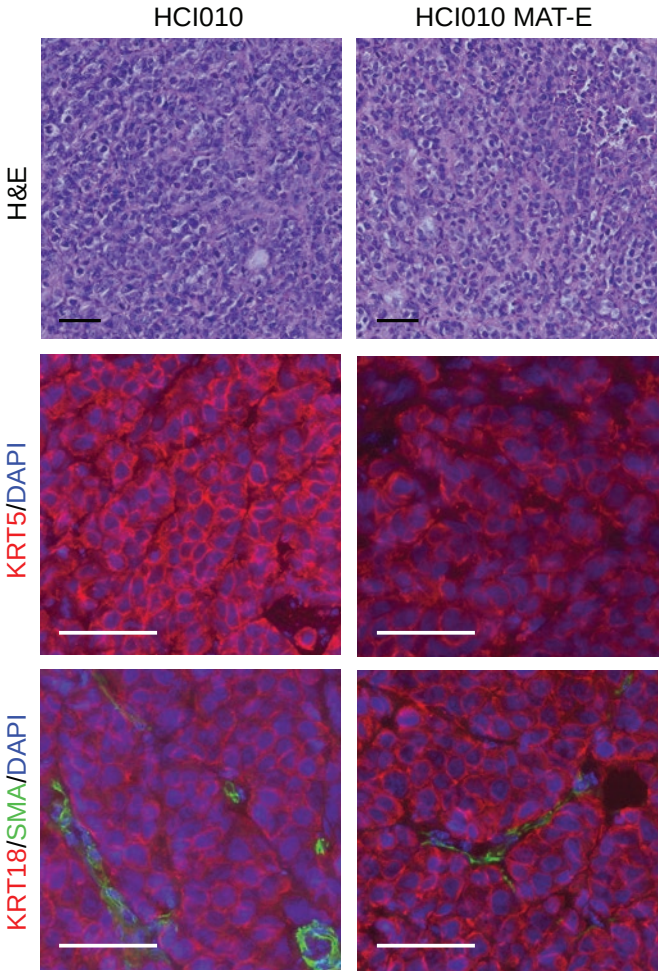

d

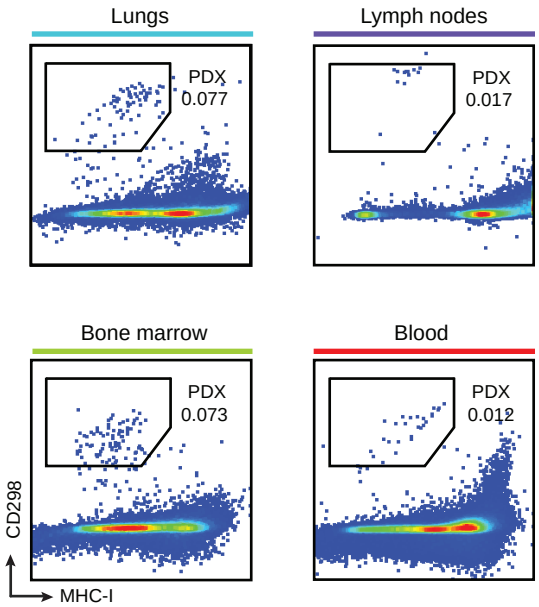

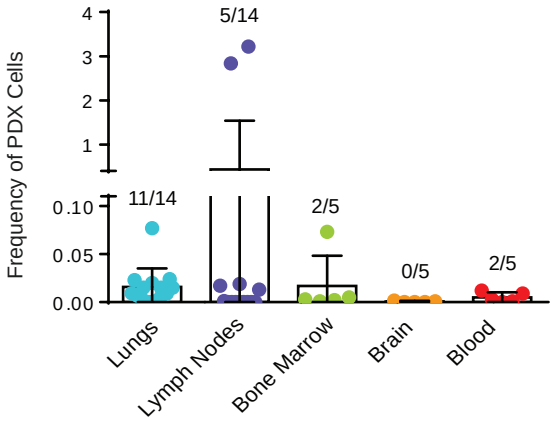

e

HCI010 MAT-E lung metastasis

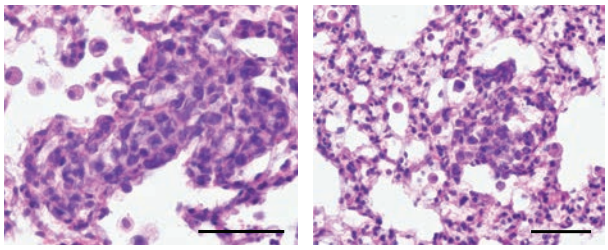

Figure 4

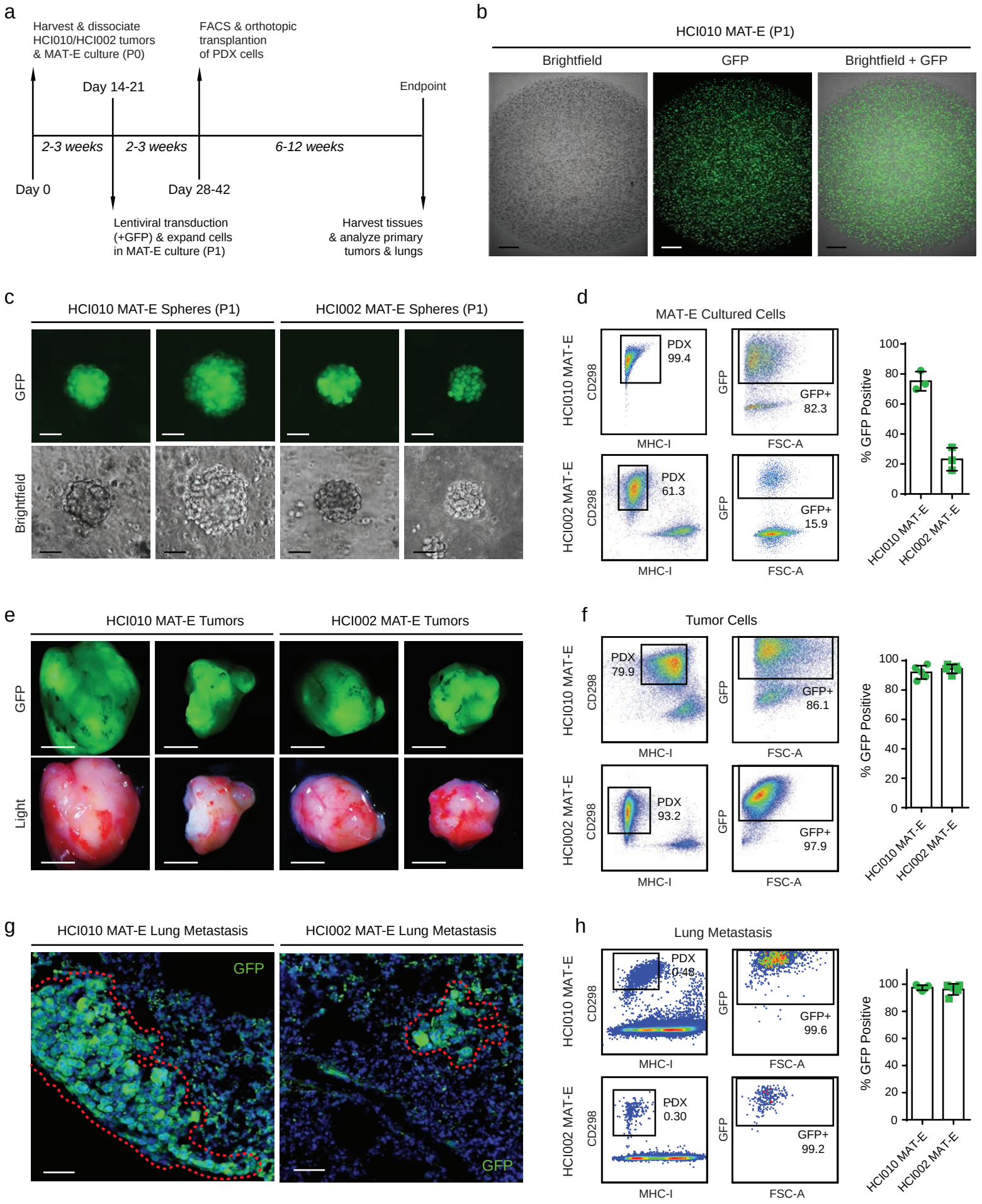
a
Harvest & dissociate HCI010/HCI002 tumors & MAT-E culture (P0)
FACS & orthotopic transplantion of PDX cells
Day 14-21
Endpoint
2-3 weeks
2-3 weeks
6-12 weeks
Day 0
Day 28-42
Lentiviral transduction (+GFP) & expand cells in MAT-E culture (P1)
Harvest tissues & analyze primary tumors & lungs
b
HCI010 MAT-E (P1)
Brightfield
GFP
Brightfield + GFP
c
HCI010 MAT-E Spheres (P1)
HCI002 MAT-E Spheres (P1)
GFP
Brightfield
d
MAT-E Cultured Cells
HCI010 MAT-E
HCI002 MAT-E
CD298
MHC-I
GFP
FSC-A
PDX 99.4
GFP+ 82.3
PDX 61.3
GFP+ 15.9
% GFP Positive
e
HCI010 MAT-E Tumors
HCI002 MAT-E Tumors
GFP
Light
f
Tumor Cells
PDX 79.9
GFP+ 86.1
PDX 93.2
GFP+ 97.9
g
HCI010 MAT-E Lung Metastasis
HCI002 MAT-E Lung Metastasis
GFP
h
Lung Metastasis
PDX 0.48
GFP+ 99.6
PDX 0.30
GFP+ 99.2

Figure 5

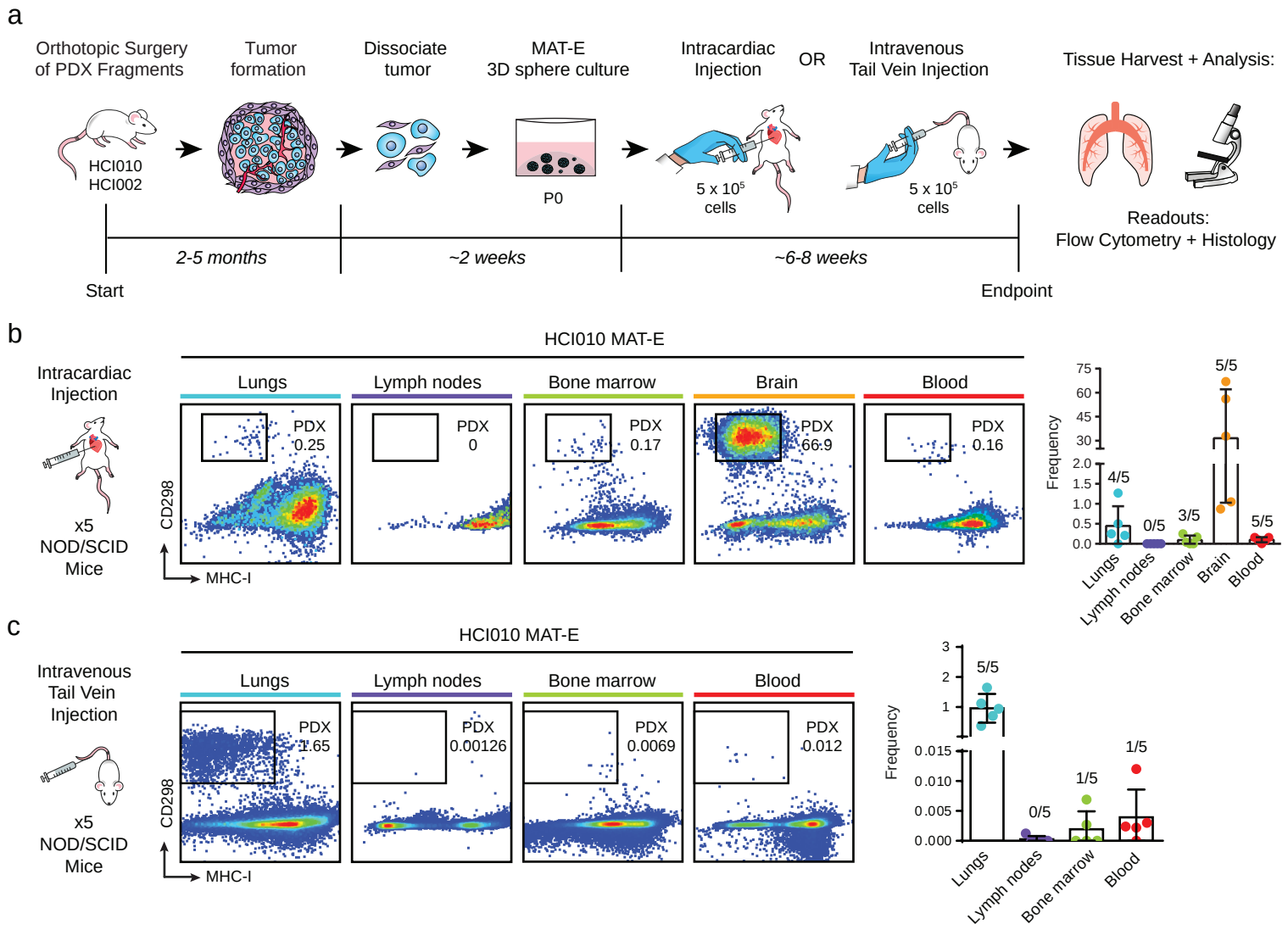
a
Orthotopic Surgery of PDX Fragments
Tumor formation
Dissociate tumor
MAT-E 3D sphere culture
Intracardiac Injection
OR
Intravenous Tail Vein Injection
Tissue Harvest + Analysis:
HCI010
HCI002
P0
5 x 10^5 cells
5 x 10^5 cells
Readouts:
Flow Cytometry + Histology
2-5 months
~2 weeks
~6-8 weeks
Start
Endpoint
b
HCI010 MAT-E
Intracardiac Injection
x5 NOD/SCID Mice
Lungs
Lymph nodes
Bone marrow
Brain
Blood
PDX 0.25
PDX 0
PDX 0.17
PDX 66.9
PDX 0.16
CD298
MHC-I
Frequency
4/5
0/5
3/5
5/5
5/5
c
HCI010 MAT-E
Intravenous Tail Vein Injection
x5 NOD/SCID Mice
Lungs
Lymph nodes
Bone marrow
Blood
PDX 1.65
PDX 0.00126
PDX 0.0069
PDX 0.012
CD298
MHC-I
Frequency
5/5
0/5
1/5
1/5
d
HCI010 MAT-E
Inset
e
HCI010 MAT-E
Keratin 5
Inset
Tumor
Lung Tissue

Figure 6

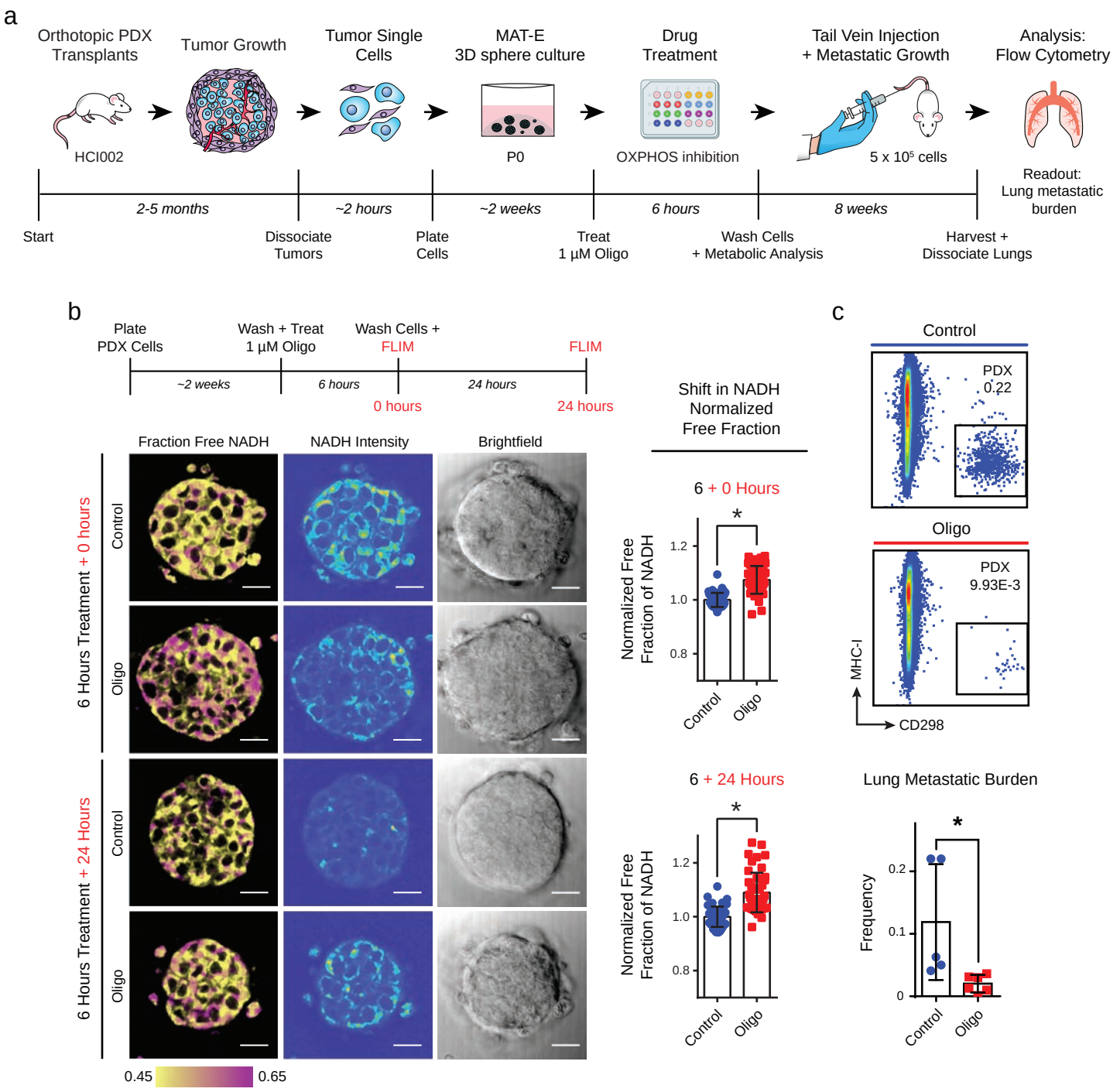
a
Orthotopic PDX Transplants
Tumor Growth
Tumor Single Cells
MAT-E 3D sphere culture
Drug Treatment
Tail Vein Injection + Metastatic Growth
Analysis: Flow Cytometry
HCI002
P0
OXPHOS inhibition
5 x 10⁵ cells
Readout: Lung metastatic burden
2-5 months
~2 hours
~2 weeks
6 hours
8 weeks
Start
Dissociate Tumors
Plate Cells
Treat 1 µM Oligo
Wash Cells + Metabolic Analysis
Harvest + Dissociate Lungs
b
Plate PDX Cells
Wash + Treat 1 µM Oligo
Wash Cells + FLIM
FLIM
~2 weeks
6 hours
24 hours
0 hours
24 hours
Fraction Free NADH
NADH Intensity
Brightfield
6 Hours Treatment + 0 hours
6 Hours Treatment + 24 Hours
Control
Oligo
0.45
0.65
Shift in NADH Normalized Free Fraction
6 + 0 Hours
6 + 24 Hours
Normalized Free Fraction of NADH
1.2
1.0
0.8
*
Control
Oligo
c
Control
Oligo
PDX 0.22
PDX 9.93E-3
MHC-I
CD298
Lung Metastatic Burden
Frequency
0.2
0.1
0

Figure 7

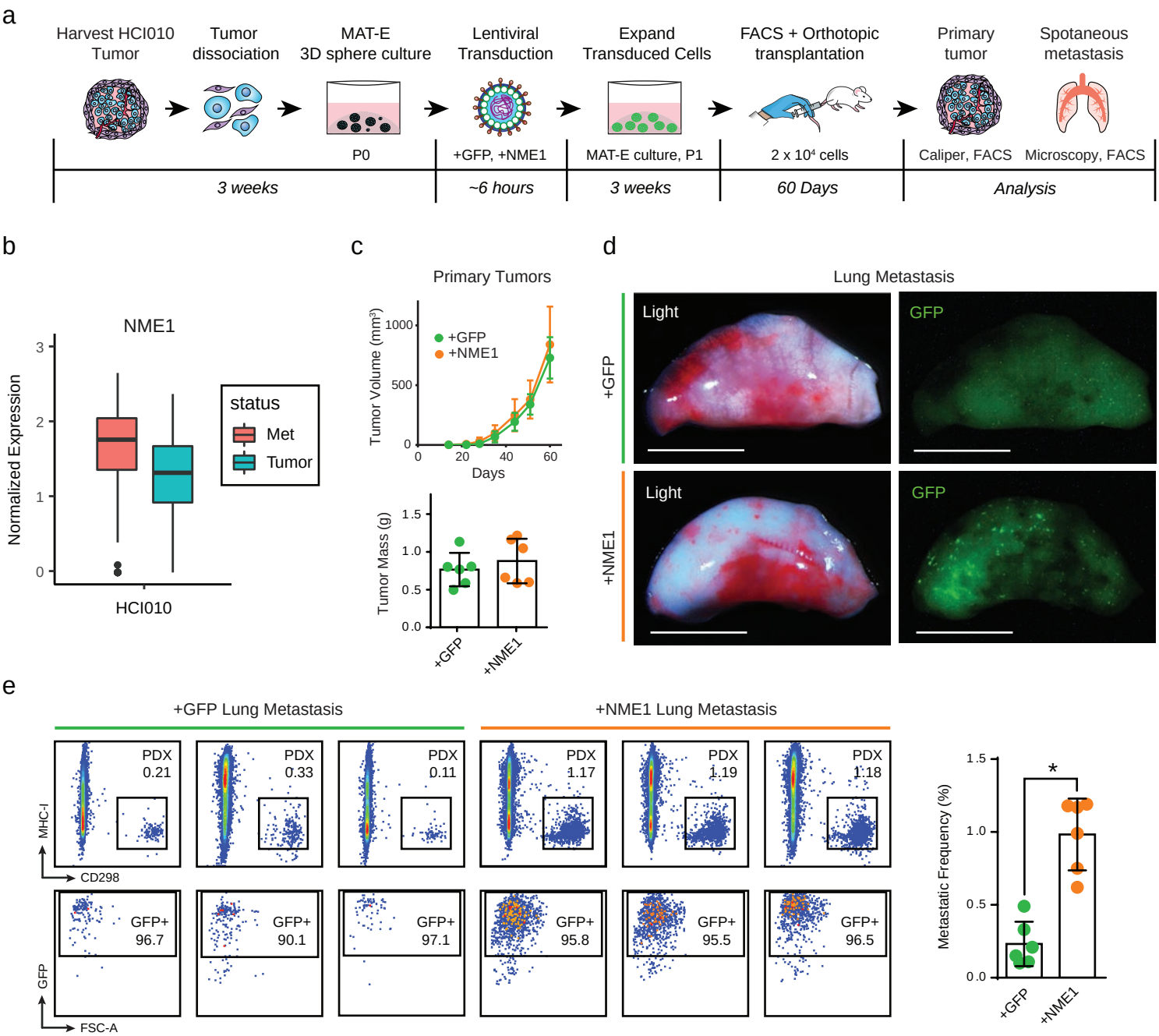
a
Harvest HCI010 Tumor
Tumor dissociation
MAT-E 3D sphere culture
Lentiviral Transduction
Expand Transduced Cells
FACS + Orthotopic transplantation
Primary tumor
Spotaneous metastasis
P0
+GFP, +NME1
MAT-E culture, P1
2 x 10⁴ cells
Caliper, FACS
Microscopy, FACS
3 weeks
~6 hours
3 weeks
60 Days
Analysis
b
NME1
Normalized Expression
status
Met
Tumor
HCI010
c
Primary Tumors
Tumor Volume (mm³)
+GFP
+NME1
Days
Tumor Mass (g)
+GFP
+NME1
d
Lung Metastasis
+GFP
+NME1
Light
GFP
e
+GFP Lung Metastasis
+NME1 Lung Metastasis
PDX 0.21
PDX 0.33
PDX 0.11
PDX 1.17
PDX 1.19
PDX 1.18
MHC-I
CD298
GFP+ 96.7
GFP+ 90.1
GFP+ 97.1
GFP+ 95.8
GFP+ 95.5
GFP+ 96.5
GFP
FSC-A
Metastatic Frequency (%)
*
+GFP
+NME1

Supplementary Figure 1

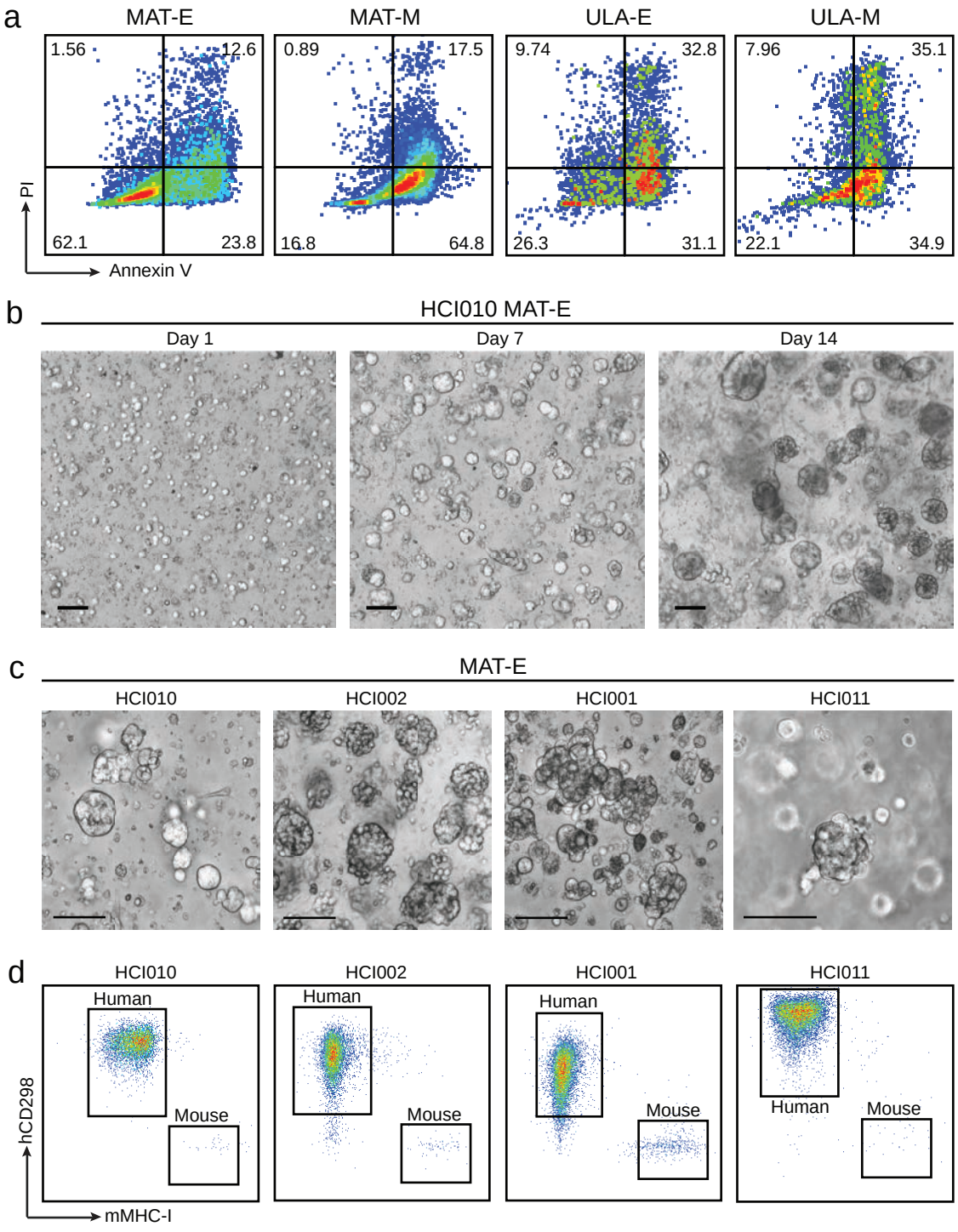

Supplementary Figure 2

a

PDX model	Cell number	Tumor frequency
HCI002 MAT-E	5.0×10^3	8/9
HCI002 MAT-E	1.0×10^4	10/10
HCI002 MAT-E	1.0×10^5	12/12

HCI002 MAT-E

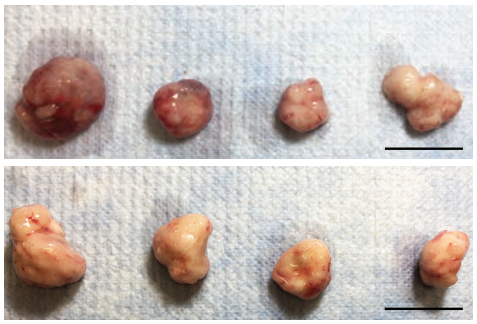

c

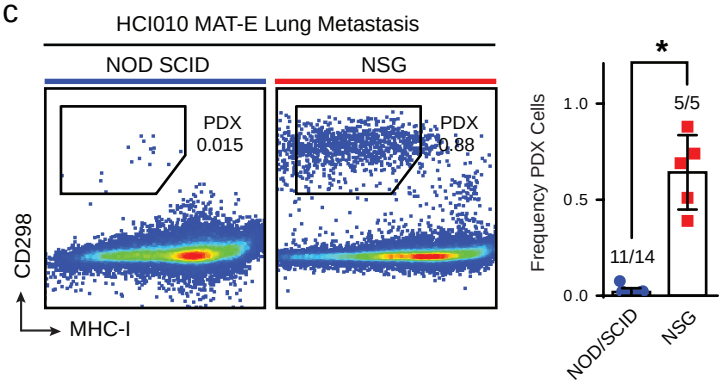

d

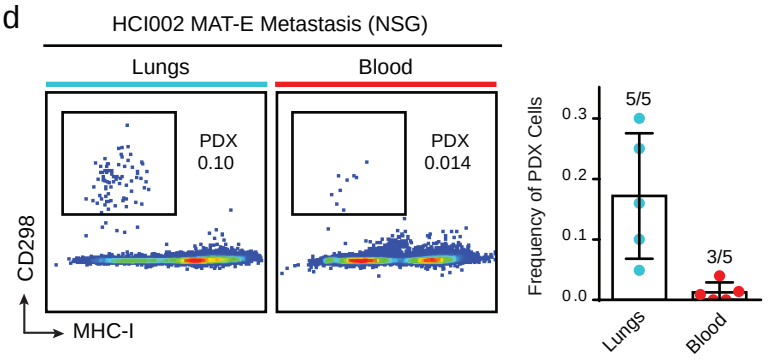

b

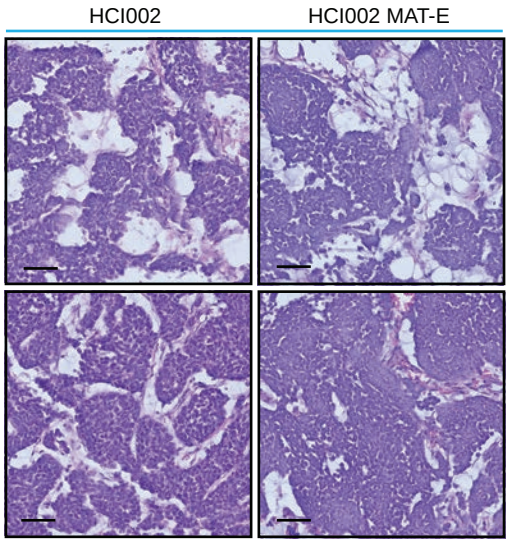

e

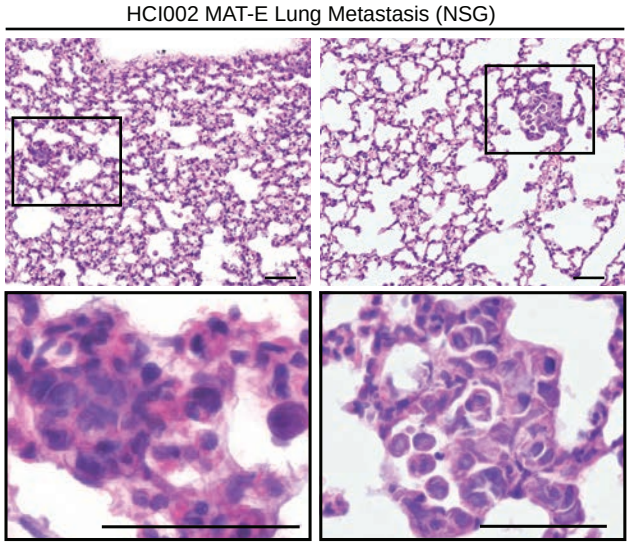

Supplementary Figure 3

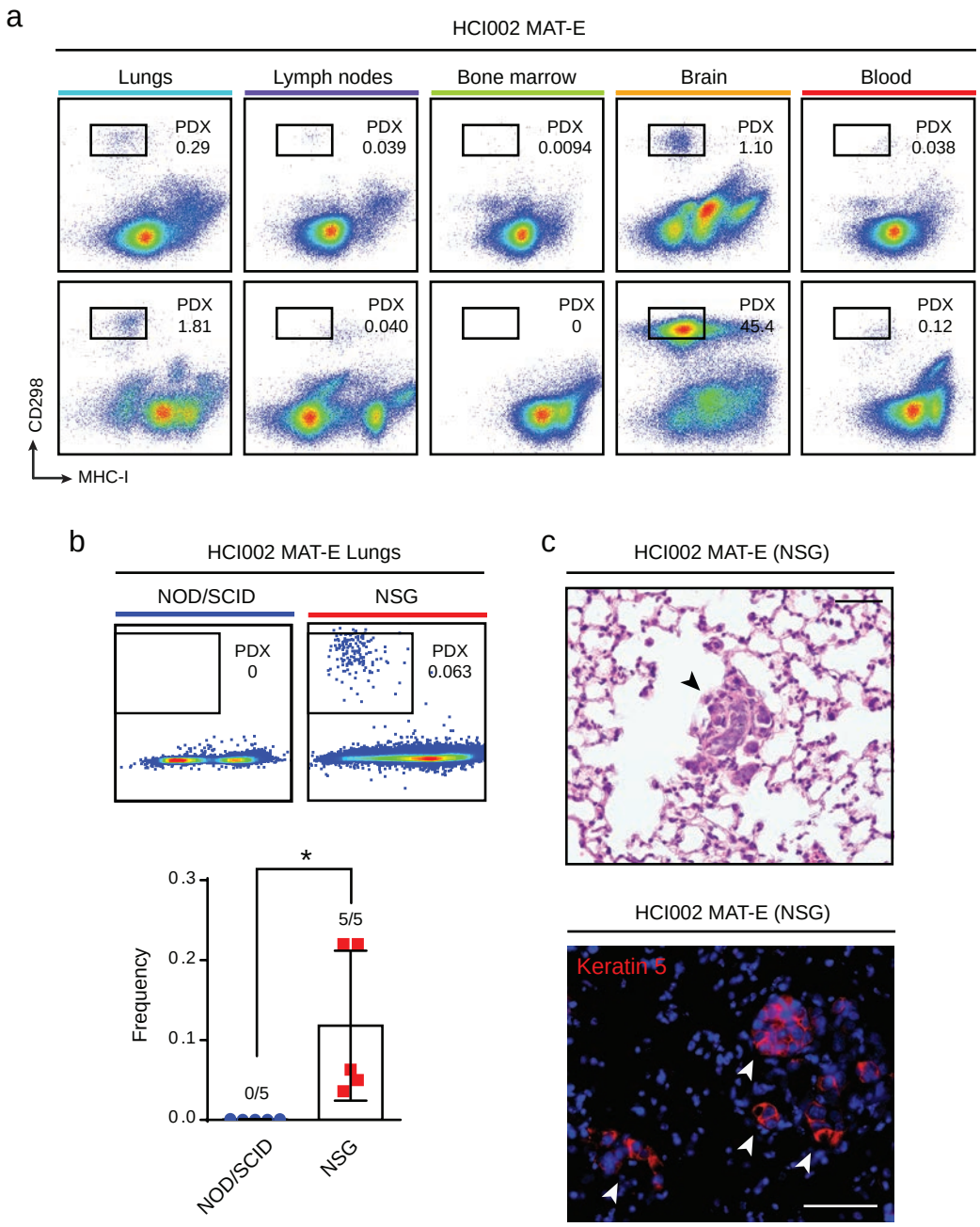

Supplementary Figure 4

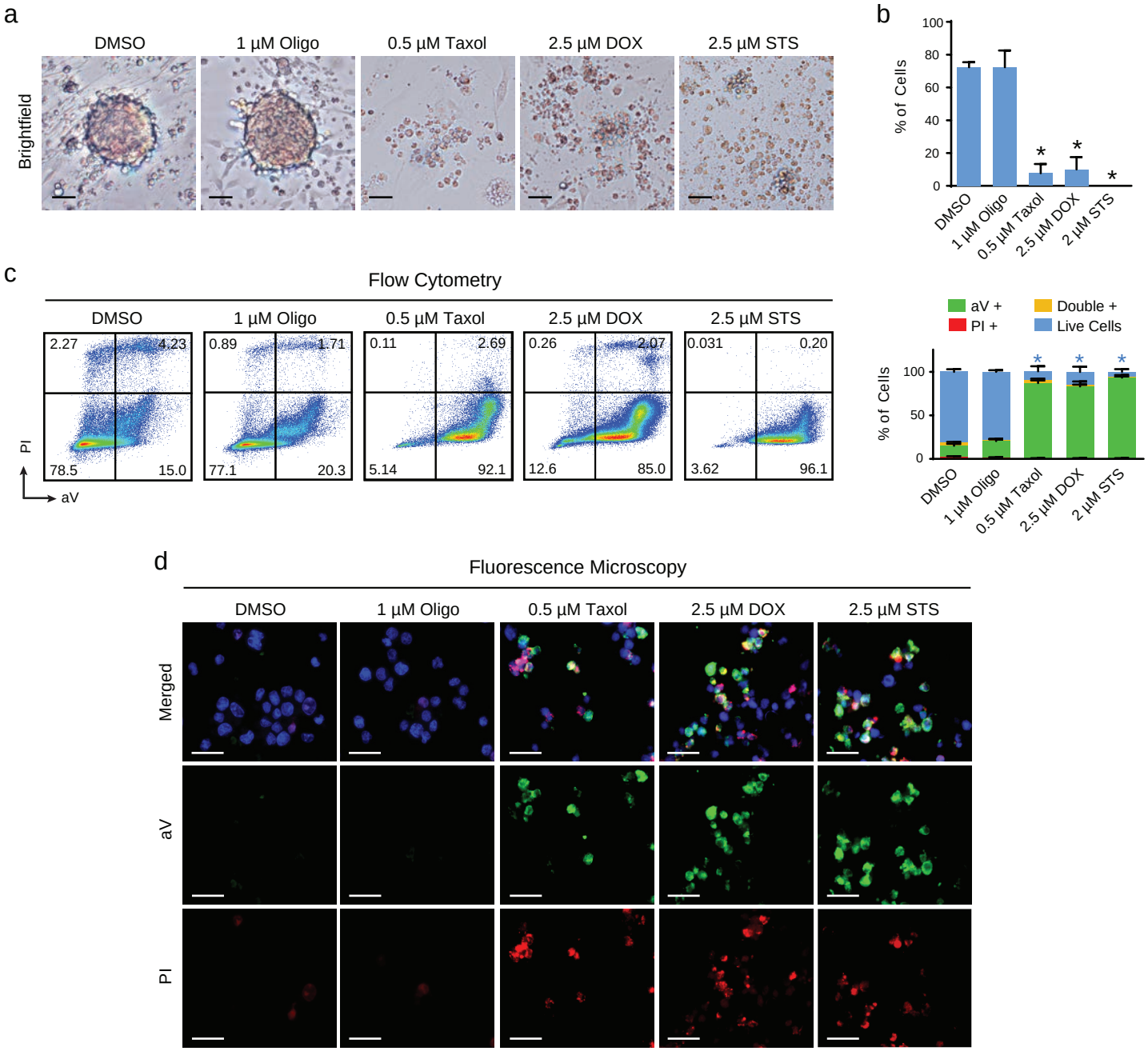
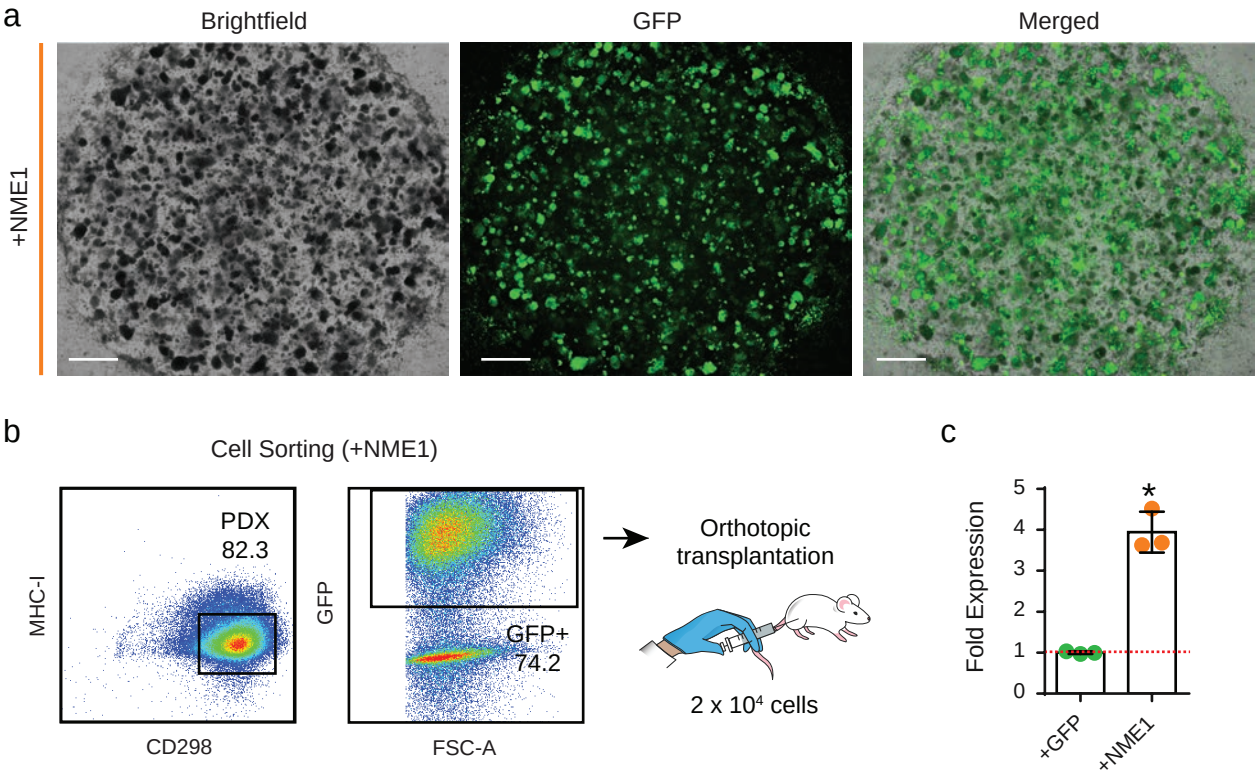
Supplementary Figure 5